Viscoelastic earthquake cycle models with deep stress-driven creep along the San Andreas fault system

K. M. Johnson and P. Segall

Geophysics Department, Stanford University, Stanford, California, USA

Received 18 March 2004; revised 15 June 2004; accepted 28 June 2004; published 5 October 2004.

[1] We develop a two-dimensional boundary element earthquake cycle model including deep interseismic creep on vertical strike-slip faults in an elastic lithosphere coupled to a viscoelastic asthenosphere. Uniform slip on the upper part of the fault is prescribed periodically to represent great strike-slip earthquakes. Below the coseismic rupture the fault creeps in response to lithospheric shear stresses within a narrow linear viscous fault zone. The model is applied to the GPS contemporary velocity field across the Carrizo Plain and northern San Francisco Bay segments of the San Andreas fault, as well as triangulation measurements of postseismic strain following the 1906 San Francisco earthquake. Previous analysis of these data, using conventional viscoelastic coupling models without stress-driven creep [*Segall*, 2002], shows that it is necessary to invoke different lithosphere-asthenosphere rheology in northern and southern California in order to explain the data. We show that with deep stress-driven interseismic creep on the San Andreas fault, the data can be explained with the same rheology for northern and southern California. We estimate elastic thickness in the range 44–100 km (95% confidence level), fault zone viscosity per unit width of $0.5–8.2 \times 10^{17}$ Pa s/m, and asthenosphere relaxation time of 24–622 years ($0.1–2.9 \times 10^{20}$ Pa s) for northern and southern California. We estimate a slip rate of 21–27 mm/yr and recurrence time of 188–315 years for the northern San Francisco Bay San Andreas fault and slip rate of 32–42 mm/yr with recurrence time of 247–536 years for the Carrizo Plain. *INDEX TERMS:* 8107 Tectonophysics: Continental neotectonics; 8159 Tectonophysics: Rheology—crust and lithosphere; 8150 Tectonophysics: Plate boundary—general (3040); *KEYWORDS:* San Andreas, slip rates, GPS

Citation: Johnson, K. M., and P. Segall (2004), Viscoelastic earthquake cycle models with deep stress-driven creep along the San Andreas fault system, *J. Geophys. Res.*, *109*, B10403, doi:10.1029/2004JB003096.

1. Introduction

[2] Interseismic deformation at the ground surface across major strike-slip faults is characterized by strain rates that are highest near the trace of the fault and decay with distance laterally away from the fault. For example, along the Carrizo Plain section of the San Andreas fault, GPS data provide the contemporary velocity distribution across the section of the fault that last ruptured in 1857 as displayed in Figure 1 (http://www.scecdc.scec.org). The data show high strain rates at the fault trace that decrease to nearly zero within about 80 km of the fault. In the San Francisco Bay area, we have both the contemporary GPS velocity field [*Prescott et al.*, 2001] and longer term deformation rates obtained by repeated triangulation surveys at Point Arena and Point Reyes [*Kenner and Segall*, 2003]. Figures 2a and 2b show the velocity distribution across the 1906 break of the San Andreas fault and the adjacent Hayward-Rodgers Creek and Concord-Green Valley faults. We again see the highest strain rates near the San Andreas and adjacent faults. Figure 2c shows a 90-year record of strain rates following the 1906 earthquake. The strain rate across the 1906 rupture was initially high after the earthquake and has been decreasing since.

[3] Several analytical models of interseismic deformation along strike-slip faults such as the San Andreas fault have been proposed, all based on the premise that the distribution of strain across a strike slip fault is a result of locking of the fault in the upper part of the lithosphere as the plates on either side of the fault move past one another. *Savage and Burford* [1973] proposed a mechanical model of interseismic strain accumulation using a buried screw dislocation in an elastic half-space (Figure 3a). In this model the mechanism by which the plates move past one another is approximated with uniform sliding on a buried vertical dislocation extending from the locking depth to infinite depth. The slip rate is prescribed to be equal to the far-field plate rate.

[4] A presumably more realistic model in which crustal deformation occurs in response to coupled viscous flow in the asthenosphere was first proposed by *Nur and Mavko* [1974]. This so-called viscoelastic coupling model consists

0148-0227/04/2004JB003096$09.00

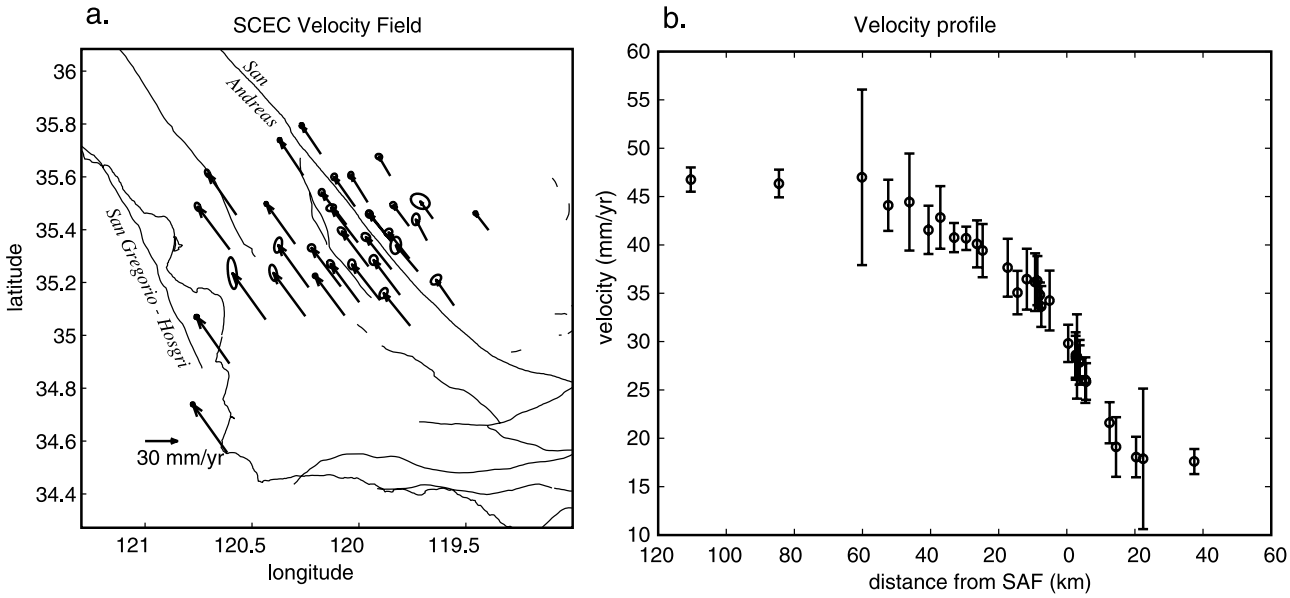

Figure 1. (a) Southern California Earthquake Center (SCEC) GPS velocities in Carrizo Plain region of southern California. (b) Projection of GPS velocities onto profile perpendicular to the San Andreas fault. Error bars are 2σ.

of a fault in an elastic lithosphere overlying a Maxwell viscoelastic half-space. Coseismic rupture on the lithospheric fault is modeled with sudden imposed displacement across a uniform dislocation. Postseismic strain accumulates in the lithosphere in response to viscous flow in the asthenosphere. *Savage and Prescott* [1978] further developed this model to include interseismic strain accumulation due to a constant far-field plate velocity resulting from an infinite sequence of periodically repeating earthquakes (Figure 3b). The *Savage and Prescott* [1978] model also incorporates steady interseismic creep on the down-dip extension of the coseismic rupture. The earthquake ruptures the lithosphere from the free surface down to depth D and creeps at a constant slip rate from depth D to the bottom of the elastic plate.

[5] Simple physical models of the creep process have been developed in which creep on the lower part of the fault is driven by stresses in the plate. *Turcotte and Spence* [1974] modeled the creeping fault as an edge crack in an elastic plate driven by loading at the ends. They ignored coupling between the elastic plate and the viscous asthenosphere. *Li and Rice* [1987] modeled the coupling between the viscous asthenosphere and elastic lithosphere through a generalized Elsasser model cast in terms of lithospheric averaged stresses and displacements in the plate. Numerical models of the dynamic process of postseismic creep, not including interseismic loading, have been developed for strike-slip faults in an elastic half-space by *Hearn et al.* [2002] and in an elastic layer coupled to a viscoelastic substrate by *Kenner and Segall* [2003] and *Linker and Rice* [1997]. Kenner and Segall developed finite element models of stress-driven postseismic creep on the San Andreas fault following the 1906 earthquake coupled to viscoelastic flow in the asthenosphere. *Parsons* [2002] developed a numerical model of the San Francisco Bay area faults including interseismic loading between earthquakes. *Reches et al.* [1994] analyzed GPS and triangulation data along the San Andreas fault using a finite element model with nonlinear crustal rheology. Numerical models must be conditioned by running the calculations through many earthquake cycles until the flow in the asthenosphere is steady state, that is the flow pattern repeats in time with the cyclic pattern of slip on the fault.

[6] *Segall* [2002] modeled the data in Figures 1 and 2 using the Savage-Prescott coupling model with $D = H$, that is, with coseismic rupture extending through the elastic plate and no interseismic creep on the fault. He showed that GPS measurements of interseismic velocities across the Carrizo Plain segment of the San Andreas fault imply a longer relaxation time (higher viscosity) than inferred from the post-1906 strain rate data recorded by triangulation surveys in the northern San Francisco Bay area. Here, relaxation time is defined as $2\eta/\mu$ where η is viscosity and μ is elastic shear modulus. Specifically, it was shown that the Savage-Prescott model places a tight lower bound of 35 years on the relaxation time of the asthenosphere in the Carrizo Plain section of the San Andreas fault while the post-1906 strain rate data places a tight upper bound of 20 years on the relaxation time. Figure 4 illustrates the sensitivity of these model parameters to the data fit. As suggested by *Segall* [2002], this discrepancy between relaxation times could be attributed to at least three causes: (1) A true difference in lithosphere-asthenosphere structure between northern and southern California, (2) nonlinear lower crust, upper mantle rheology, or (3) aseismic creep below the seismogenic part of the lithosphere. It is the latter possibility, that of triggered aseismic creep, that we investigate here.

[7] Nonlinear asthenosphere rheology would be consistent with results of laboratory experiments of ductile olivine flow which show that the effective viscosity is lower at higher strain rates [e.g., *Karato and Wu*, 1993]. Indeed,

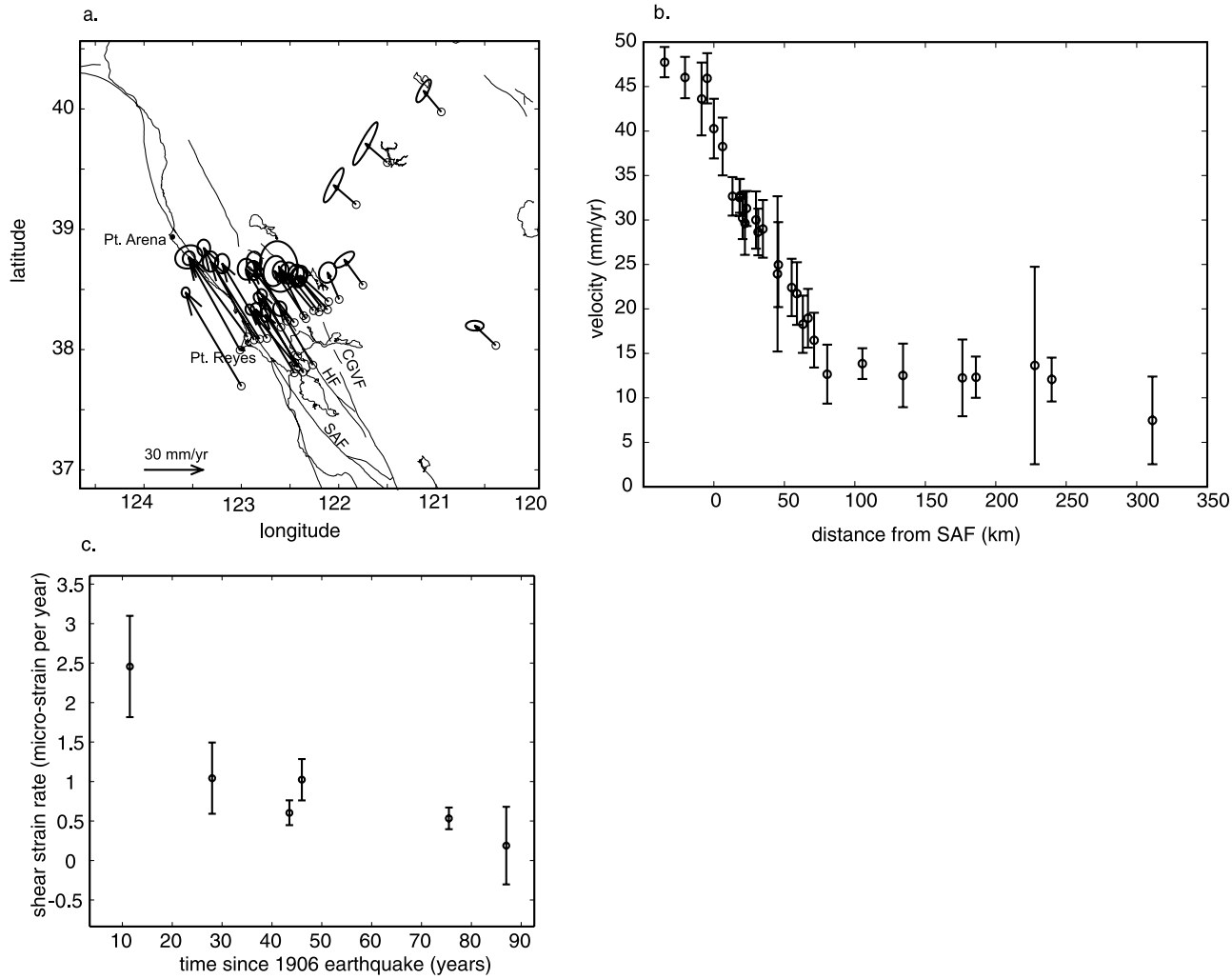

Figure 2. (a) GPS velocities in northern San Francisco Bay region of California [*Prescott et al.*, 2001]. SAF, San Andreas fault; HF, Hayward fault; CGVF, Concord-Green Valley fault. (b) Projection of GPS velocities onto profile perpendicular to the San Andreas fault. Error bars are 2σ. (c) Triangulation and trilateration measurements of post-1906 strain rate transient [*Kenner and Segall*, 2003]. Error bars are 2σ.

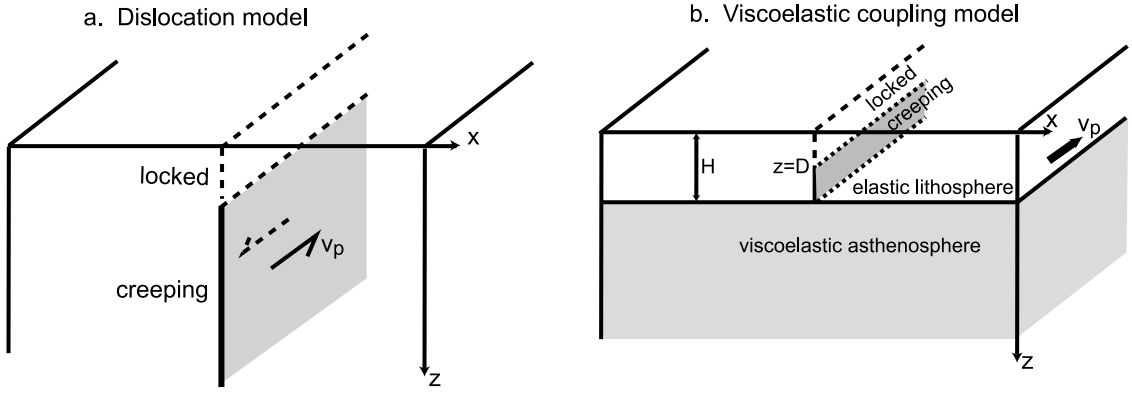

Figure 3. (a) Savage-Burford model. Interseismic deformation is modeled as slip on a buried dislocation that slides at the plate rate, V_p. (b) Savage-Prescott coupling model. Cyclic motion down to depth D and steady sliding below D on a fault in an elastic layer over viscoelastic half-space. Slip rate on the fault is equal to the plate velocity, V_p.

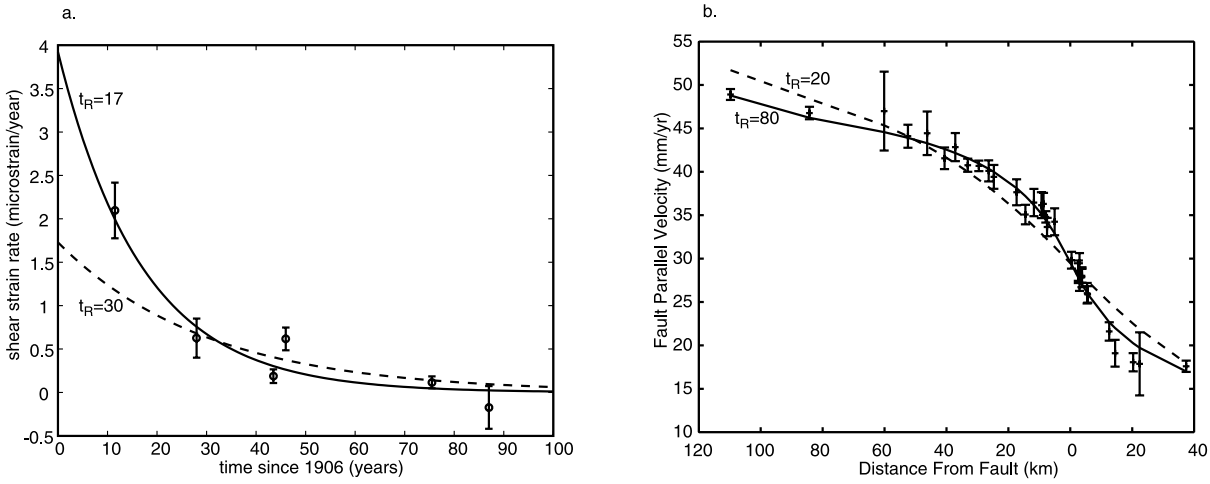

Figure 4. (a) Fit to post 1906 strain rate data using Savage-Prescott viscoelastic coupling (Figure 3b) model for two values of t_R. Optimal value is t_R = 17. Poor fit with t_R = 30 demonstrates the ability of the data and model to place an upper bound of about 25 years on t_R. (b) Fit to Carrizo Plain data using Savage-Prescott model for two values of t_R. Optimal value is t_R = 80. Poor fit with t_R = 20 demonstrates the ability of the data and model to place a lower bound on values of t_R at about 30 years.

Pollitz et al. [2001] inferred nonlinear upper mantle viscosity from modeling of interferometric synthetic aperture radar data following the Hector Mine, California, earthquake. They showed that the observations could best be explained with a time-varying viscosity that is initially low after the earthquake and increases with time.

[8] Aseismic creep on a discrete fault zone underlying the coseismic rupture plane is also a likely mechanism. *Kenner and Segall* [2003] showed that the post-1906 strain rate transient is reproduced with postseismic slip within a discrete vertical shear zone underlying the coseismic rupture. They fit the data with a creeping fault in an elastic lithosphere overlying a viscoelastic half-space with a 200 year relaxation time. Furthermore, seismic tomography suggests that the major faults in the San Francisco Bay extend well below the cutoff depth of seismicity as a discrete zone [*Henstock et al.*, 1997; *Parsons*, 1998; *Parsons and Hart*, 1992]. A similar result has been reported for the San Andreas fault in southern California by *Zhu* [2000].

[9] In this paper, we show that different relaxation times (viscosities) in northern and southern California are not necessary to explain the GPS and triangulation data if the fault below the coseismic rupture responds as a linear viscous shear zone. We develop boundary element models of interseismic deformation with stress-driven creep in the lower lithosphere coupled to viscoelastic flow in the asthenosphere. Several different models of interseismic creep on the fault in the lower lithosphere are tested against the geodetic data. While other researchers have produced various mechanical models of deep creep on strike-slip faults, we choose to use the boundary element approach because it has the advantage of incorporating the coupling of the lithosphere and asthenosphere exactly without the computational expense of finite element calculations.

[10] We begin our analysis by comparing four different viscoelastic coupling models of interseismic deformation along strike-slip faults (Figure 5). The first is the "no-creep" model of *Savage and Prescott* [1978] in which the coseismic fault breaks the entire elastic plate without interseismic creep on the fault. This was the model used by *Segall* [2002] to analyze the San Andreas fault data. The second is the kinematic "constant-creep" model of *Savage and Prescott* [1978] in which the fault is locked interseismically to a depth D and creeps at an imposed constant rate (equal to the plate velocity) from depth D to the bottom of the elastic plate. The other two models incorporate stress-driven creep through application of boundary element techniques. In the "constant-stress" model, the fault creeps at a constant resistive shear stress below depth D throughout the earthquake cycle. In the "viscous-creep" model, the fault below depth D responds as a linear viscous shear zone.

2. Viscoelastic Coupling Models

[11] All of the coupling models in this paper are based on the notion of an idealized earthquake cycle. The models consist of periodic motion on an infinitely long fault represented by a dislocation in a two-dimensional elastic layer overlying a Maxwell viscoelastic half-space (Figure 5). Sudden slip imposed at regular time intervals from the Earth's surface to depth D represents great strike-slip earthquakes. Between depths D and H the fault creeps. The long-term slip is uniform over the entire depth of the fault. The coseismic rupture and aseismic creep load the viscoelastic asthenosphere, which relaxes at a rate determined by the relaxation time (equal to $2\eta/\mu$, where η is viscosity and μ is shear modulus). The asthenosphere flows to relax the stresses induced by fault slip and in turn reloads the elastic lithosphere. After an infinite number of earthquakes, the asthenosphere flow is steady state, such that the flow pattern repeats in time with the cyclic slip pattern on the fault, and the constant far-field velocity of the lithosphere is equal to the long-term slip rate on the fault.

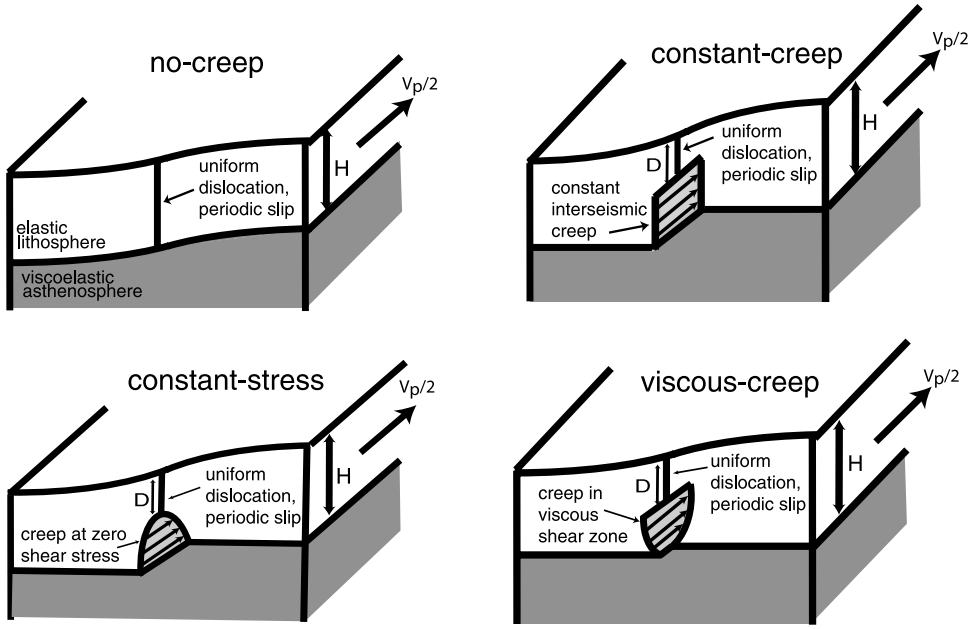

Figure 5. Coupling models. No creep, coseismic rupture breaks entire elastic plate. Constant creep, creeping part of fault slides at constant slip rate. Constant stress, creeping part slides at constant (zero) resistive shear stress. Viscous creep, creeping part deforms as linear viscous shear zone.

[12] We recognize that the notion of a periodic earthquake cycle is highly idealized. For example, the historical record and paleoseismic evidence suggests that earthquakes are not truly periodic but are instead clustered in time [e.g., *Grant and Sieh*, 1994]. The concept of the earthquake cycle is a simplified representation of the strain accumulation and release process, as central to elastic rebound theory, that is certain to be more complicated and irregular in nature. In addition, two-dimensional models can not consider the effects of earthquakes on other segments of the fault. However, if the recurrence times and slip rates in the cycle models are considered to be representative of the average frequency and magnitude of large strike-slip earthquakes, then useful information can be gleaned about this process through comparison of theoretical models and geodetic data.

2.1. Savage-Prescott Constant Fault Creep Model

[13] In the *Savage and Prescott* [1978] model (Figure 3b), creep between depths D and H on the fault is imposed at a constant rate, which we take to be equal to the far-field plate rate. This cycle model builds on the solution for a single earthquake on a fault in an elastic layer over a viscoelastic half-space first presented by *Nur and Mavko* [1974]. For the fault extending from the surface to depth D in an elastic layer of thickness H with shear modulus μ overlying a viscoelastic half-space with the same elastic shear modulus and viscosity, η, the velocity field due to a single earthquake with slip Δu is

$$v(x,z) = \frac{\Delta u}{\pi t_R} e^{-t/t_R} \sum_{n=1}^{\infty} \frac{(t/t_R)^{n-1}}{(n-1)!} F_n(x,z,D,H), \qquad (1)$$

where t is time since the earthquake, $t_R = 2\eta/\mu$ is relaxation time of the half-space, Δu is the coseismic slip magnitude, and

$$\begin{aligned} F_n(x,z,D,H) = & \frac{1}{2}\tan^{-1}\left(\frac{x}{z-2nH+D}\right) \\ & -\frac{1}{2}\tan^{-1}\left(\frac{x}{z-2nH-D}\right) \\ & +\frac{1}{2}\tan^{-1}\left(\frac{x}{z+2nH+D}\right) \\ & -\frac{1}{2}\tan^{-1}\left(\frac{x}{z+2nH-D}\right). \end{aligned} \qquad (2)$$

For velocities at the ground surface ($z = 0$), the expression for F_n simplifies to

$$F_n(x,z=0,D,H) = \tan^{-1}\left(\frac{x}{2nH-D}\right) - \tan^{-1}\left(\frac{x}{2nH+D}\right). \qquad (3)$$

Savage and Prescott [1978] formed the earthquake cycle by superposition as illustrated in Figure 6a. Periodic back-slip motion (equal to minus the long-term slip rate) down to depth D is added to steady sliding at the long-term rate on the entire fault. This produces a locked fault with periodic, sudden slip events down to depth D and steady sliding below depth D. The steady forward sliding simply produces a dislocation of the elastic plate in which the two sides move at constant velocity equal to half the plate rate. The periodic back slip perturbs the steady velocity field, producing time-dependent deformation associated with locking and unlocking of the upper part of the fault.

[14] We formulate a solution equivalent to the Savage and Prescott solution without application of the back-slip con-

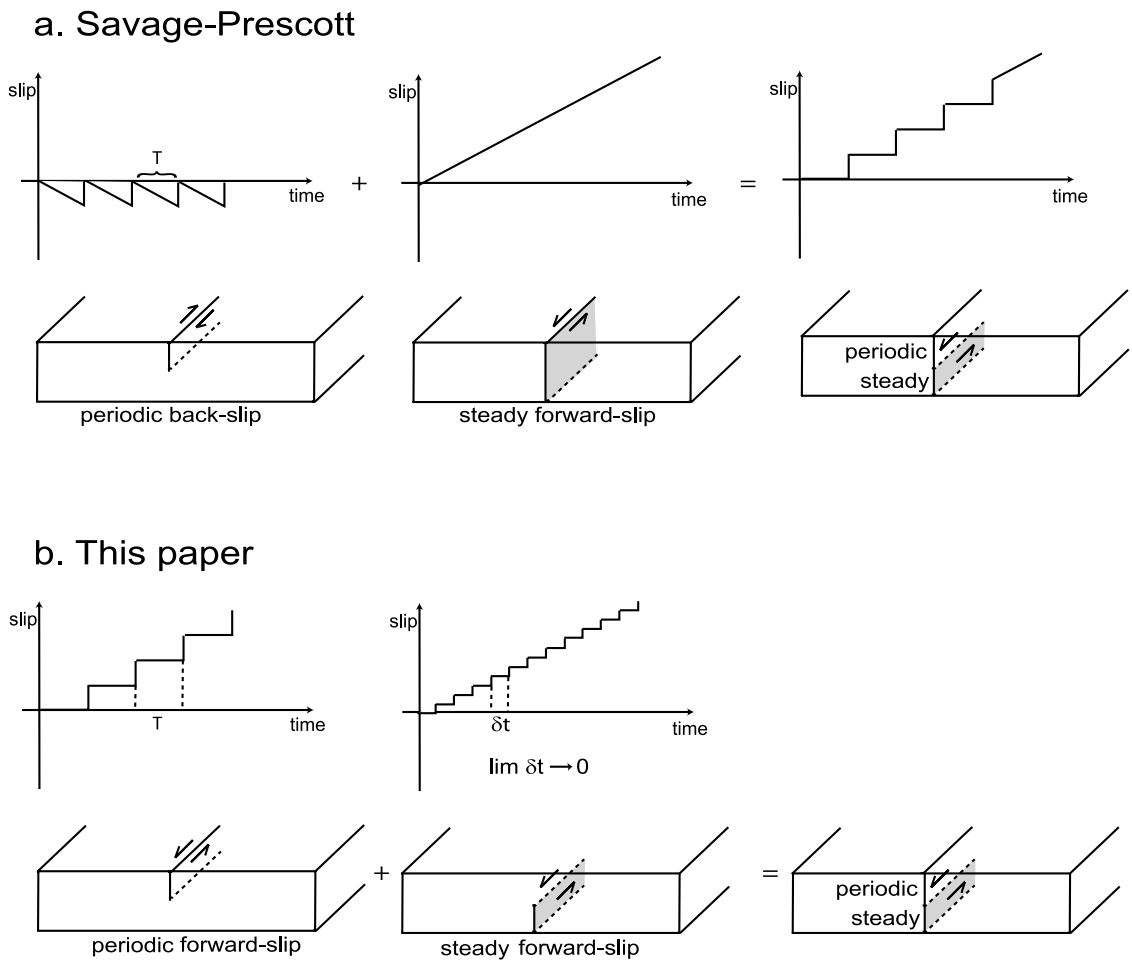

Figure 6. (a) Superposition used by *Savage and Prescott* [1978] to obtain the coupling model. (b) Superposition used in this paper to obtain the coupling model. Regardless of the solution method, periodic slip occurs on part of fault extending to depth D. Between D and H the fault creeps at constant slip rate equal to the plate rate.

cept as illustrated in Figure 6b. We sum separate solutions for cyclic motion on the fault down to depth D and steady sliding from depth D to H. The cyclic motion is obtained by summing an infinite number of Nur-Mavko earthquakes (equations (1) and (2) or (3)) spaced at regular time intervals of duration T and occurring at times $-kT$ for k ranging from 0 to ∞,

$$v(x,t) = \frac{\dot{s}T}{\pi t_R} e^{-t/t_R} \sum_{n=1}^{\infty} \Phi_n(t/t_R, T/t_R) F_n(x, D, H), \qquad (4)$$

where

$$\Phi_n(t/t_R, T/t_R) = \frac{1}{(n-1)!} \sum_{k=0}^{\infty} e^{-kT/t_R} \left(\frac{t+kT}{t_R}\right)^{n-1}. \qquad (5)$$

Here $\dot{s}$ is the long-term slip rate, t_R is the relaxation time of the asthenosphere, t is observation time, and T is recurrence interval. The slip, Δu, in equation (1) has been replaced by $\dot{s}T$.

[15] For practical application of equation (1), the infinite sum over n is truncated and higher order terms are approximated with steady slip on a buried dislocation in an elastic half-space as shown by *Savage* [1990]. See Appendix A for details. For small n, the infinite sum over k in equation (5) can be done analytically.

[16] The solution for steady sliding can be thought of as the sum of many single earthquake events with slip $\Delta u = \dot{s}T$ in the limit as the time between events, T, approaches zero. The velocity due to creep from the surface to depth D, $v_c^{0,D}$, is calculated using equations (4) and (5) by replacing kT/t_R with τ and T/t_R with $d\tau$ and integrating over τ,

$$v_c^{0,D}(x,t) = \frac{\dot{s}}{\pi} \sum_{n=1}^{\infty} \frac{F_n(x,D,H)}{(n-1)!} \int_0^{\infty} e^{-\tau} \left(\frac{t}{t_R} + \tau\right)^{n-1} d\tau. \qquad (6)$$

This is the expression for the velocity at time $t > 0$ due to creep at a constant rate, $\dot{s}$, during the time interval $t = -\infty$ to $t = 0$. For the solution at time $t = 0$, we must add in the elastic component of the velocity,

$$v_c^{0,D}(x, t=0) = \frac{\dot{s}}{\pi} \sum_{n=1}^{\infty} \frac{F_n(x,D,H)}{(n-1)!} \int_0^{\infty} e^{-\tau} (\tau)^{n-1} d\tau + \frac{\dot{s}}{\pi} \tan^{-1}\left(\frac{x}{D}\right). \qquad (7)$$

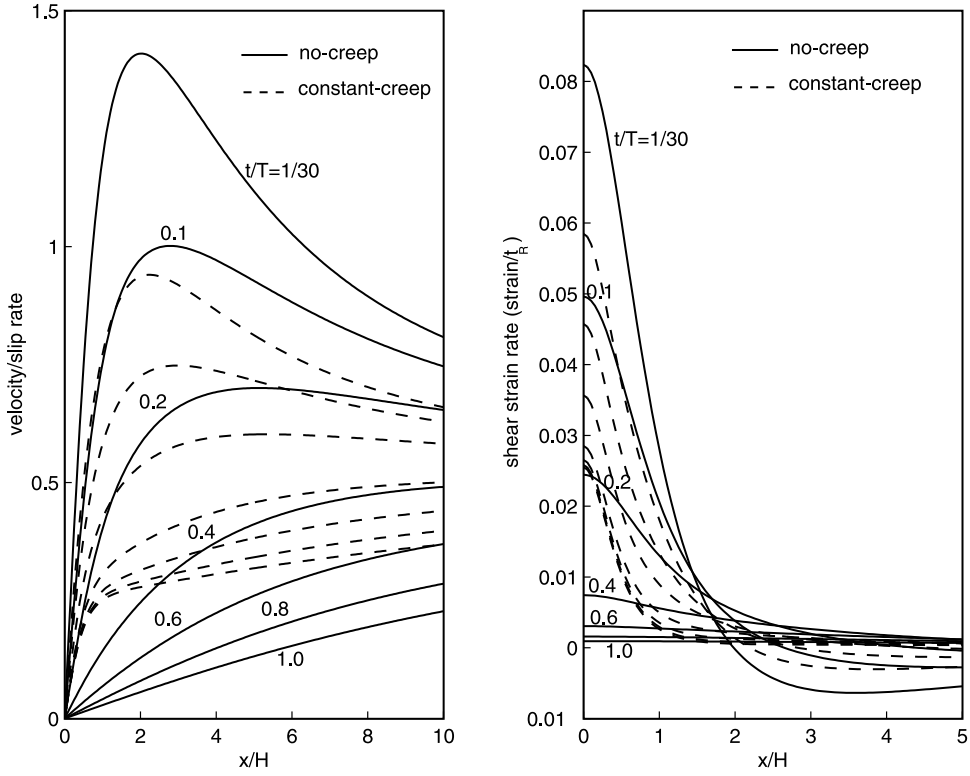

Figure 7. Comparison of velocity and strain rates for no-creep model ($D = H$) and constant-creep model with $T = 10t_R$, $D = 0.5H$, at various times, t/t_R, throughout the cycle. The no-creep model displays higher strain rates early in the cycle and lower strain rates later in the cycle.

The term on the far right side of equation (7) is the solution for a uniform dislocation extending from the surface to depth D in an elastic half-space. The integral in equation (7) is the well-known gamma function which, for integer n, is [*Abromowitz and Stegun*, 1970]

$$\int_0^\infty e^{-\tau}(\tau)^{n-1}d\tau = (n-1)!. \tag{8}$$

Therefore the solution for the creeping fault simplifies to

$$v_c^{0,D}(x) = \frac{\dot{s}}{\pi}\sum_{n=1}^{\infty} F_n(x,D,H) + \frac{\dot{s}}{\pi}\tan^{-1}\left(\frac{x}{D}\right). \tag{9}$$

The solution for the velocities, $v_c^{D,H}$, due to creep from depth D to depth H is obtained from the superposition of creep at rate $\dot{s}$ from the surface to depth H and creep at rate $-\dot{s}$ from the surface to depth D,

$$\begin{aligned} v_c^{D,H}(x) &= v_c^{0,H} - v_c^{0,D} \\ &= \frac{\dot{s}}{2}\mathrm{sgn}(x) - \frac{\dot{s}}{\pi}\sum_{n=1}^{\infty} F_n(x,D,H) - \frac{\dot{s}}{\pi}\tan^{-1}\left(\frac{x}{D}\right). \end{aligned} \tag{10}$$

The final solution for the earthquake cycle, the sum of equations (4) and (10), is equivalent to that given by *Savage and Prescott* [1978]. We obtain strain rate by taking the derivative of velocity with respect to the spatial coordinate, x.

[17] The original question we posed was whether interseismic creep below the coseismic rupture can account for the discrepancy in asthenosphere relaxation times inferred by *Segall* [2002]. Segall showed that if there is no fault creep, it is necessary to have lower relaxation time in northern California than in southern California to explain the high strain rates following the 1906 San Francisco earthquake and the contemporary velocity field across the Carrizo Plain. We thus compare strain rates from the no-creep model with strain rates from the constant-creep model. Figure 7 compares strain rates at the ground surface near the fault calculated from the constant-creep [*Savage and Prescott*, 1978] model ($D = 0.5H$) with the no-creep model ($D = H$). For the sake of comparison we use the same values of T/t_R and t/t_R as *Segall* [2002], where T is earthquake repeat time and t is time since the last quake. *Segall* [2002] inferred a recurrence interval of about 300 years for the northern San Francisco Bay San Andreas fault and asthenosphere relaxation time of about 30 years. Assuming these values, the high strain rate observation at about 10 years after the 1906 earthquake is at $t/T = 1/30$. As shown in Figure 7, assuming these cycle parameters, the strain rate at $t/T = 1/30$ is actually lower in the constant-creep model than the no-creep model. Thus the constant-creep model would actually require a relaxation time shorter than 30 years to produce the observed high strain rates, making the discrepancy between the southern California and northern California asthenosphere relaxation times larger.

[18] These results suggest that constant fault creep cannot account for the discrepancy in asthenosphere relaxation times along the San Andreas fault. Clearly, in order to fit

the initial high strain rates without a short asthenosphere relaxation time, it is necessary that the fault creep faster than the plate rate. Indeed, rapid afterslip well above the plate rate has been inferred from postseismic deformation following numerous large earthquakes [e.g., *Burgmann et al.*, 2002; *Hsu et al.*, 2002]. The lower creeping part of the fault experiences high shear stress immediately after coseismic rupture due to coseismic stress loading and rapid relaxation of the asthenosphere. Later in the cycle, the shear stresses acting on the fault are lower as the asthenospheric flow becomes less vigorous and the coseismic stress has relaxed. Therefore, if we allow creep to be driven by shear stresses acting on the fault, we would expect high slip rates early in the cycle and low slip rates late in the cycle, as was found by *Li and Rice* [1987]. Below we develop two models which incorporate stress-driven, time-dependent creep, including rapid afterslip.

2.2. Creep at Constant Resistive Shear Stress

[19] Perhaps the simplest model for stress-driven creep is slip on the fault at constant (equivalently, zero) resistive shear stress [e.g., *Li and Rice*, 1987]. An integral equation for the slip distribution at any given time is obtained by setting equal to zero the sum of the stresses acting on the creeping part of the fault due to (1) slip on the creeping fault and (2) repeated slip on the upper, interseismically locked portion of the fault. Both contributions include the stressing due to coupled asthenospheric flow. Consider a fault locked to depth D and creeping from depth D to H. Let $\sigma(z, t)$ be the "driving stress" at depth z and time t, set up by repeated slip on the upper part of the fault. Let $g(z, \xi, t - t_{\text{slip}})$ be the stress acting on the creeping part of the fault at depth z and time t due to a point dislocation source on the creeping fault with unit slip at time t_{slip} located at depth ξ. We assume the slip pattern on the creeping fault is cyclic with period T, thus the point source solution is cyclic with period T. The time varying part of the deformation field is independent of the value of the resistive stress, so we integrate the stresses on the creeping fault over the length of the fault (from H to D) and over an entire earthquake cycle (from $-T + t$ to t), add this to the driving stress and set the sum equal to zero

$$\int_{-T+t}^{t}\int_{H}^{D} g(z,\xi,t-\tau)B(\xi,\tau)d\xi d\tau + \sigma(z,t) = 0, \qquad (11)$$

where B is the Burger's vector distribution of slip rate (spatial gradient of the slip rate),

$$B = \frac{\partial^2 s}{\partial \xi \partial \tau}.$$

There do not appear to be analytical solutions to equation (11). We therefore find a numerical solution for the slip distribution employing a boundary element method, using the cycle solution previously derived. We discretize the creeping fault into n patches of uniform slip and equal length and discretize the earthquake cycle into m equal time intervals, Δt. The slip is calculated at times $t_i = i\Delta t$ with earthquake rupture occurring at time $t_m = m\Delta t$. The slip on each patch at all times is related to the stresses on the patches through the system of equations

$$\begin{pmatrix} V_m+E & V_{m-1} & V_{m-2} & V_{m-3} & \cdots & V_1 \\ V_1 & V_m+E & V_{m-1} & V_{m-2} & \cdots & V_2 \\ V_2 & V_1 & V_m+E & V_{m-1} & \cdots & V_3 \\ V_3 & V_2 & V_1 & V_m+E & \cdots & V_4 \\ \vdots & & & & & \\ V_{m-1} & V_{m-2} & V_{m-3} & V_{m-4} & \cdots & V_m+E \end{pmatrix} \cdot \begin{pmatrix} s_1 \\ s_2 \\ s_3 \\ s_4 \\ \vdots \\ s_m \end{pmatrix} + \begin{pmatrix} \sigma_1 \\ \sigma_2 \\ \sigma_3 \\ \sigma_4 \\ \vdots \\ \sigma_m \end{pmatrix} = 0. \qquad (12)$$

The σ_i are $n \times 1$ vectors containing the stresses in the ith time interval on n patches induced by repeated coseismic slip down to depth D. The s_i are vectors containing the slip on all n patches at the ith time interval,

$$s_i = \begin{pmatrix} s_i^1 \\ s_i^2 \\ \vdots \\ s_i^n \end{pmatrix}, \sigma_i = \begin{pmatrix} \sigma_i^1 \\ \sigma_i^2 \\ \vdots \\ \sigma_i^n \end{pmatrix}. \qquad (13)$$

In this notation, subscripts denote time indices, while superscripts denote spatial indices. The V_i are $n \times n$ matrices relating the viscoelastic contribution of the stresses acting on the patches during the ith time interval to slip on the patches, and E is a matrix relating the instantaneous, elastic contribution of the stresses due to slip on the patches.

[20] The viscoelastic component of stresses on the center of the jth fault patch due to unit slip on the kth patch extending from depth $D1_k$ to $D2_k$ at time t_i is

$$V_i(j,k) = \frac{\mu}{\pi}\sum_{n=1}^{\infty}\Phi_n(t_i/\tau_R, T/\tau)[W_n(D2_k) - W_n(D1_k)], \qquad (14)$$

where

$$W_n(D_k) = \frac{D - 2Hn + z_j}{(D - 2Hn + z_j)^2 + x_j^2} - \frac{D + 2Hn + z_j}{(D + 2Hn + z_j)^2 + x_j^2} + \frac{-D + 2Hn + z_j}{(-D + 2Hn + z_j)^2 + x_j^2} - \frac{-D - 2Hn + z_j}{(-D - 2Hn + z_j)^2 + x_j^2}, \qquad (15)$$

(x_j, z_j) is the location of the center of the jth patch, Φ is defined in equation (5), and μ is elastic shear modulus. The stresses in equation (14) are obtained by differentiating the velocities (equations (4) and (2)) with respect to the spatial coordinate, x, to obtain strain rate, multiplying by shear modulus, μ, to convert to stress rate, and then integrating over the duration of the time interval to obtain the stress accumulated during the time interval. The stresses due to repeated slip on the seismogenic part of the fault, σ_i, are obtained in the same way.

[21] The elastic component of stresses simply come from the solution for a screw dislocation in an elastic half-space. The elastic stress on the center of the jth fault patch due to

unit slip on the kth patch extending from depth $D1_k$ to $D2_k$ is

$$E(j,k) = \frac{\mu}{2\pi}\left(\frac{z_j + D2_k}{(z_j + D2_k)^2 + x_j^2} - \frac{z_j - D2_k}{(z_j - D2_k)^2 + x_j^2} - \frac{z_j + D1_k}{(z_j + D1_k)^2 + x_j^2} + \frac{z_j - D1_k}{(z_j - D1_k)^2 + x_j^2}\right). \quad (16)$$

Writing equation (12) in the form

$$Gs + \sigma_d = 0, \quad (17)$$

we obtain the slip distribution by numerically inverting G

$$s = -G^{-1}\sigma_d. \quad (18)$$

[22] Figure 8 is a plot of the cumulative interseismic slip and slip rate at regularly spaced time intervals throughout an earthquake cycle with $T = 10t_R$, and $D = 0.5H$. For unit coseismic slip down to depth D, the coseismic slip tapers from unity at depth D to zero at depth H (Figure 8a). During the interseismic phase, slip on the creeping fault accumulates as the asthenosphere relaxes from the coseismic stress change and as interseismic strain accumulates in the lithosphere (Figures 8a and 8b). At the end of a complete cycle, the slip on the creeping fault has slipped uniformly 1 unit. As expected, the slip rate is high early in the cycle and low late in the cycle (Figure 8c).

[23] Figure 9 compares the surface velocity and shear strain rate at various times for the constant-stress model with $D = 0.5H$ and the no-creep model. The velocity and shear strain rates are higher at early times in the no-creep model because the coseismic rupture extends uniformly to the bottom of the lithosphere while the coseismic slip is tapered to the bottom in the constant-stress model. Coseismic rupture in the no-creep model therefore induces larger stresses on the top of the asthenosphere that are rapidly relaxed early in the cycle. Later in the cycle the shear strain rates and velocities are higher in the constant-stress model because slip on the creeping part of the fault places the deformation closer to the surface. While the ratio D/H was chosen rather arbitrarily for this example, the pattern of higher shear strain rates in the no-creep model early in the cycle and lower rates later in the cycle holds regardless of the choice of this ratio.

[24] As was the case in the previous constant-creep model, the constant-stress model cannot account for the discrepancy noted by *Segall* [2002] in the northern and southern California asthenosphere relaxation times. As discussed above, if we assume the cycle parameters inferred by *Segall* [2002], the high strain rate observation 10 years after the 1906 earthquake is at time $t/T = 1/30$. We see that the constant-stress model predicts lower strain rate at time $t/T = 1/30$ than the no-creep model. So as the case with the constant-creep model, the constant-stress model would require the northern California asthenosphere relaxation time to be shorter than estimated by *Segall* [2002] using the no-creep model. This again would make the discrepancy between northern and southern California even larger.

[25] In section 2.3 we explore a model in which the coseismic rupture extends part way through the elastic plate with rapid afterslip and interseismic creep in a linear viscous fault zone.

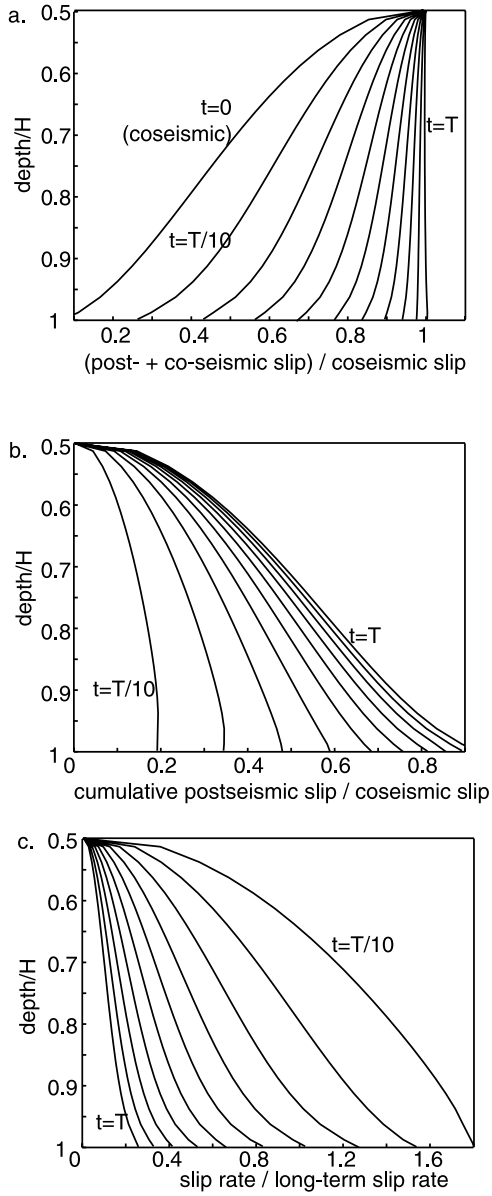

Figure 8. Cumulative interseismic slip distribution and slip rates for constant-stress model at 10 uniformly spaced time intervals. $T = 10t_R$, $D = 0.5H$. (a) Cumulative coseismic and postseismic/interseismic slip. (b) Cumulative postseismic/interseismic slip. (c) Slip rate at each time interval.

2.3. Linear Viscous Shear Zone

[26] In order to include the effects of rapid postseismic afterslip immediately below the coseismic rupture, we model the creeping portion of the fault as a linear viscous shear zone [e.g., *Linker and Rice*, 1997; *Hearn et al.*, 2002; *Kenner and Segall*, 2003]. The linear creep law is

$$\dot{s} = \frac{h}{\eta_f}\sigma, \quad (19)$$

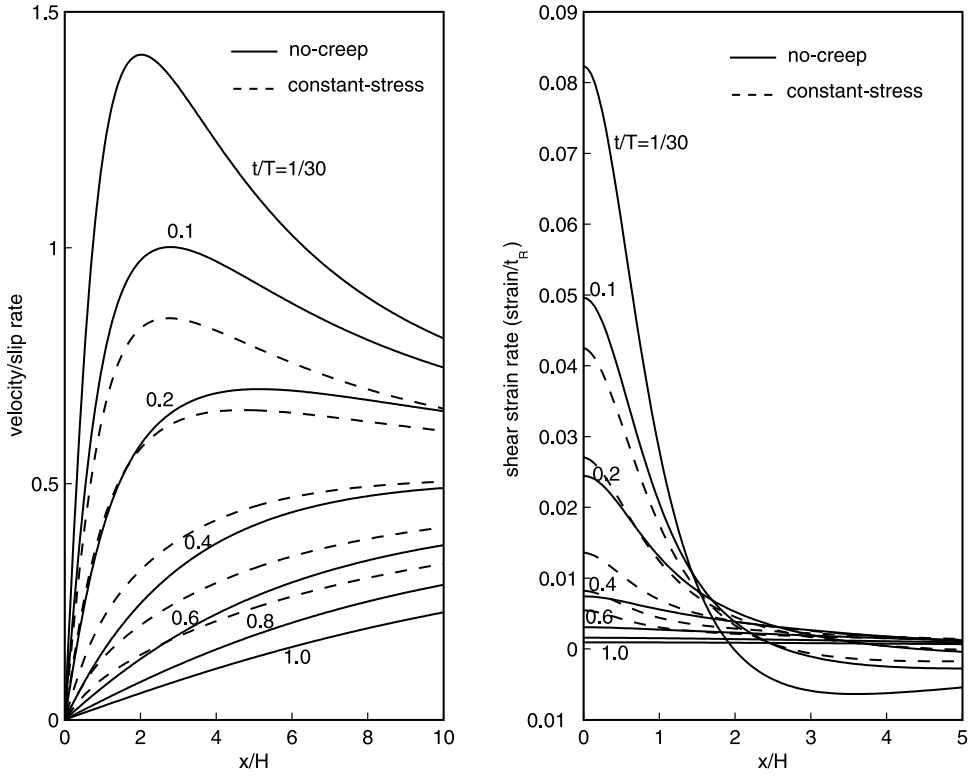

Figure 9. Comparison of velocity and strain rates for constant-stress model (with $D = 0.5H$) and no-creep model ($D = H$). $T = 10t_R$ for both models.

where η_f and h are the viscosity and width of the fault zone, respectively, and $\dot{s}$ and σ are again the slip rate and shear stress, respectively, on the creeping part of the fault. Note in this constitutive formulation, we assume a fault zone of finite width which deforms in simple shear. We have chosen a linear rheology for the fault zone so that we can superimpose solutions to simulate the earthquake cycle. However, there is reason to believe that the fault responds nonlinearly to stress perturbations. For example, rate-and-state friction predicts that slip rate depends exponentially on stress. Several studies have modeled creep following large earthquakes using the rate-and-state constitutive formulation [e.g., *Linker and Rice*, 1997; *Lapusta et al.*, 2000; *Hearn et al.*, 2002].

[27] If we discretize the problem exactly as in section 2.2, the vector of incremental stresses acting on patches of the creeping fault is $Gs + \sigma_d$, where G is the matrix in equation (12), σ_d is again the driving stress due to repeated slip on the seismogenic part of the fault, and s is again the vector of incremental slip on each patch during each time interval. The slip rate in equation (19), however, is proportional to the total stress acting on the patch during the time interval. So we convert from incremental stress to total stress by transforming $(Gs + \sigma_d)$ such that the ith row of the new matrix is the sum of the first i rows of $(Gs + \sigma_d)$. That is, we construct the vector $L(Gs + \sigma_d)$, where L is the lower triangular matrix

$$\begin{pmatrix} I_{n\times n} & 0 & 0 & \cdots & 0 \\ I_{n\times n} & I_{n\times n} & 0 & \cdots & 0 \\ I_{n\times n} & I_{n\times n} & I_{n\times n} & \cdots & 0 \\ \vdots & & & & \\ I_{n\times n} & I_{n\times n} & I_{n\times n} & \cdots & I_{n\times n} \end{pmatrix}$$

and $I_n \times {}_n$ is the $n \times n$ identity matrix.

[28] Replacing σ in equation (19) with $L(Gs + \sigma_d)$, the discretized system of equations is

$$\dot{s} = \frac{h}{\eta_f}(LGs + L\sigma_d). \tag{20}$$

To solve for $\dot{s}$, we rearrange equation (20) as

$$\left(\frac{\eta_f}{h}I - LG\delta t\right)\dot{s} = L\sigma_d, \tag{21}$$

where δt is the length of the time interval and I is the identity matrix. We then invert the system to obtain the slip rate on each patch at every time interval

$$\dot{s} = \left(\frac{\eta_f}{h}I - LG\delta t\right)^{-1} L\sigma_d. \tag{22}$$

The accuracy of the solution improves with decreasing size of δt. We have found that $\delta t = T/100$ is sufficiently small, as smaller time steps do not significantly change the calculated slip distribution.

[29] If the viscosity of the fault zone is zero, there is no resistive shear stress and we expect to recover the constant-stress solution. We can easily show that this is the case. For $\eta_f = 0$,

$$\dot{s} = -\frac{1}{\delta t}(LG)^{-1}L\sigma_d = -\frac{1}{\delta t}G^{-1}L^{-1}L\sigma_d,$$

or

$$s = -G^{-1}\sigma_d.$$

[30] Figure 10 shows the cumulative slip and slip rate at various times during an earthquake cycle with $T = 10t_R$, $D =$

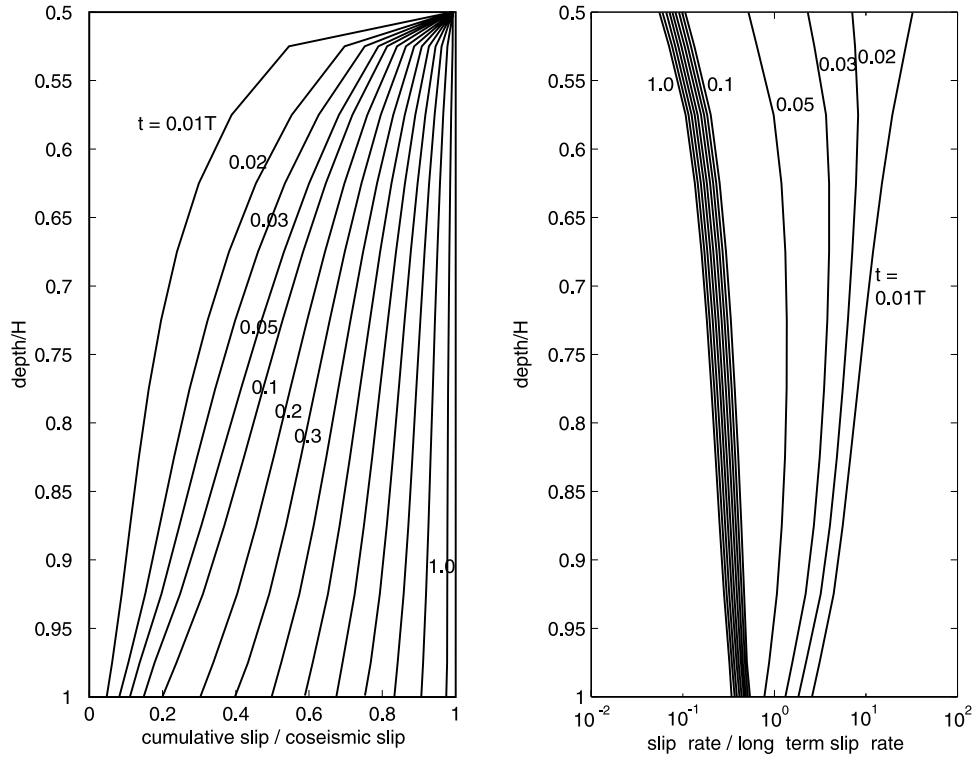

Figure 10. Cumulative slip distribution and slip rate at various times for viscous fault zone model with $\eta_f/h = 0.1\ \eta_h$, $T = 10t_R$, $D = 0.5H$. Note that time intervals are not uniform.

$0.5H$, and $\eta_f/h = 0.01\eta_h/h$, where η_h is viscosity of half-space. Because the deeper part of the shear zone does not rupture coseismically, there is rapid afterslip in the early part of the cycle below the coseismic rupture which acts to relax the coseismic stresses. We again compare this model with the no-creep model to evaluate the possibility that this mechanism may account for the apparent northern-southern California viscosity discrepancy. Figure 11 compares surface velocities and strain rates for the no-creep model ($D = H$) and the viscous fault zone model. The shear strain rates at the fault trace are higher throughout the cycle in the viscous fault zone model. The higher strain rates early in the cycle are due to the rapid afterslip at the top of the creeping zone. Late in the cycle the strain rates are higher in the viscous-creep model because slip on the fault brings the deformation closer to the surface.

[31] These results suggest that the viscous-creep model may account for the discrepancy noted by *Segall* [2002] in the northern and southern California asthenosphere relaxation times. As discussed above, if we assume the cycle parameters inferred by *Segall* [2002], the high strain rate observation at about 10 years after the 1906 earthquake is at time $t/T = 1/30$. We see that the viscous-creep model predicts higher strain rate at time $t/T = 1/30$ than the no-creep model. Thus the viscous-creep model may fit the triangulation data with a higher asthenosphere viscosity than inferred by *Segall* [2002].

3. Analysis of San Francisco Bay and Carrizo Plain Data Using Viscous Fault Zone Model

[32] We now apply the viscous-creep model to deformation data along the San Andreas fault. We are partly motivated by the previous study of *Kenner and Segall* [2003] to simultaneously model the postseismic triangulation data and interseismic GPS data using the viscous-creep boundary element model. *Kenner and Segall* [2003] showed that the post-1906 strain rate transient is reproduced with postseismic slip within a discrete vertical shear zone underlying the coseismic rupture. They fit the data with a creeping fault in an elastic lithosphere overlying a viscoelastic half-space with a 200 year relaxation time, suggesting the low relaxation time inferred by *Segall* [2002] is not necessary to explain the data. *Kenner and Segall* [2003] subtracted the interseismic strain rate from the triangulation data and modeled only the postseismic transient signal. The interseismic rate was removed with a buried Savage-Burford dislocation model (Figure 3a) assuming an interseismic slip rate determined from GPS data. It is, of course, more natural to analyze the interseismic and postseismic data with a consistent model. Here, we are able to analyze the total transient signal because the model developed in section 2.3 explicitly includes interseismic strain accumulation.

3.1. The 1906 Postseismic and Carrizo Plain Interseismic Data

[33] We begin by modeling the 1906 postseismic data shown in Figure 2c and the Carrizo Plain GPS velocities shown in Figure 1. The San Andreas fault is approximated as an infinitely long vertical strike-slip fault locked during the interseismic period down to 10 km depth and creeping in a viscous shear zone below 10 km. The 10 km locking depth was chosen based on slip inversions for large earthquakes in California [e.g., *Murray et al.*, 1993; *Mathews and Segall*, 1993; *Jonsson et al.*, 2002]. In these estimates of coseismic slip, most of the slip is concentrated above

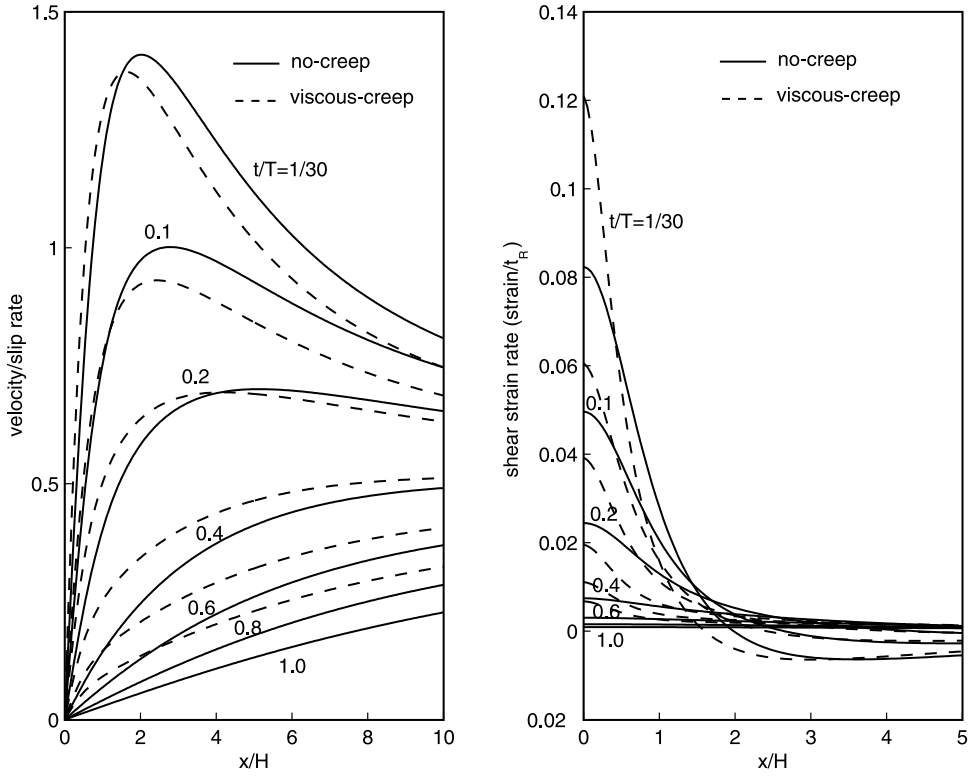

Figure 11. Comparison of velocity and strain rate at various times throughout the earthquake cycle with $T = 10t_R$ and $D = 0.5H$ for constant-creep and viscous-creep models. The fault zone viscosity is $\eta_f = 0.1\eta_h$.

10 km depth. In order to address the question of whether the geodetic data in northern and southern California can be explained with the same lithosphere/asthenosphere rheology, we assume the same elastic thickness, half-space and fault zone viscosity, and locking depth for the northern and southern sections of the San Andreas fault. We invert the data with a priori bounds on parameters similar to *Segall* [2002]. All estimated and assumed parameters as well as the a priori bounds are listed in Table 1. Lower bounds on recurrence times, T, come from the historical record of past earthquakes (1906 San Francisco earthquake in San Francisco Bay, 1857 Fort Tejon earthquake in Carrizo Plain). The upper bounds on recurrence times are set such that coseismic slip is not excessively large. The bounds on the northern San Andreas fault slip rate are based loosely on the northern California *Working Group on California Earthquake Probabilities (WGCEP)* [1999], and the conservative bounds on Carrizo Plain slip rates are based on estimates of geologic rates determined by *Sieh and Jahns* [1984].

[34] The a priori constraints on the model parameters are enforced through a Bayesian formulation of the inverse problem. The boundary element solution outlined above gives a nonlinear functional relationship between the vector of model parameters, **m**, and the vector of data, **d**,

$$\mathbf{d} = g(\mathbf{m}). \tag{23}$$

The a posteriori probability density function of the model parameters, σ, given the constraint by the data is

$$\sigma(\mathbf{m}|\mathbf{d} = g(\mathbf{m})) = k\rho_M(\mathbf{m})\rho_D(g(\mathbf{m})), \tag{24}$$

where k is a constant, ρ_M is the a priori probability density function for the model parameters, and ρ_D is the probability density function of the model parameters given only the information from the data [*Mosegaard and Tarantola*, 2002].

[35] To find the a posteriori distribution, we use a Monte Carlo-Metropolis method [e.g., *Mosegaard and Tarantola*,

Table 1. A Priori Bounds for Carrizo Plain

Parameter	Symbol	Minimum	Maximum
Elastic thickness	H	10	100
Half-space relaxation time, years	t_R	none	500
Bay area San Andreas fault recurrence interval, years	T_n	100	500
Carrizo Plain San Andreas fault recurrence interval, years	T_s	150	600
Bay area San Andreas fault slip rate, mm/yr	$\dot{S}_n$	19	27
Carrizo Plain San Andreas fault slip rate, mm/yr	$\dot{S}_s$	31	42
Fault zone viscosity per unit width, Pa s/m	η_f	none	none
Locking depth, km	D	10	10 (fixed)
Time since 1906 earthquake, years	t_n	93	93 (fixed)
Time since 1857 earthquake, years	t_s	136	136 (fixed)

Table 2. Carrizo Plain Inversion Results

Parameter	A Priori Bounds	95% Confidence	Most Probable
H, km	10–100	44–100	60
t_R, years	none	24–622	24 (1.1×10^{19})
T_n, years	100–500	208–458	275
T_s, years	150–600	316–539	350
$\dot{s}_n$, mm/yr	19–27	19.7–27	27
$\dot{s}_s$, mm/yr	31–42	31.8–41.6	36.5
η_f, Pa s/m	none	$(0.5–8.2) \times 10^{17}$	0.5×10^{17}

2002]. We assume box functions for the a priori distributions, $\rho_M(m)$, on slip rate and recurrence time. That is, the distributions are constant within the bounds listed in Table 1 and zero outside the bounds. We assume uniform a priori distributions for the other parameters. To sample the a posteriori distribution, σ, we initiate a random walk through the model space that samples the a priori distribution. The random walk is a so-called Markov Chain random walk in which the probability of visiting the model $\mathbf{m}_j$, given that the current model is $\mathbf{m}_i$, depends only on $\mathbf{m}_i$ and not on previously visited models. The model $\mathbf{m}_j$, with d unknowns, is generated randomly from $\mathbf{m}_i$ as follows:

$$\mathbf{m}_j = \mathbf{m}_i + \sum_{k=1}^{d} \alpha_k r_k \mathbf{e}_k, \tag{25}$$

where r_k is a $(-1, 1)$ uniform random deviate, $\mathbf{e}_k$ is the unit vector along the kth axis in parameter space, and α_k scales the step size along coordinate directions and is determined empirically as discussed below. To sample the a posteriori distribution, this random walk is directed with a so-called Metropolis step. The random walk does not automatically move from $\mathbf{m}_i$ to $\mathbf{m}_j$. The walk moves to the next model with probability

$$P_{ij} = \min\left(1, \frac{\rho_D(g(\mathbf{m}_j))}{\rho_D(g(\mathbf{m}_i))}\right). \tag{26}$$

If the model $\mathbf{m}_j$ is not accepted, a new random step is generated from $\mathbf{m}_i$.

[36] We have found if α_k is too large the randomly generated models are accepted at a low rate and the algorithm is inefficient. If α_k is too small, the random walk may get trapped in a local minimum and not adequately explore the high probability regions of the parameter space. Thus we vary α_k until the algorithm appears to be running efficiently. When this is the case, the algorithm accepts about 25–50% of the random models.

[37] The results of the inversion are summarized in Table 2 and Figure 12, and the fit to the data is shown in Figure 13. The viscosities of the fault zone and asthenosphere are each resolved to within about an order of magnitude. The fault zone viscosity per unit width, $0.5–8.2 \times 10^{17}$ Pa s/m (95% confidence interval), is at least an order of magnitude lower than the asthenosphere viscosity, $0.1–2.9 \times 10^{20}$ Pa s. The elastic thickness ranges from 44 to 100 km. The slip rates are not well resolved. The probability distribution of the slip rates is quite broad across the entire a priori interval. The recurrence times are somewhat better resolved. The northern Bay San Andreas recurrence interval is in the range 200–470 years and the Carrizo Plain recurrence interval is in the range 330–550 years.

[38] We see in Figure 13 that all the data are fit within the 2σ error bars. So we have indeed verified that it is not necessary with this model to have a lower relaxation time in northern California than in southern California as concluded by *Segall* [2002] using the no-creep model.

[39] For comparison, we show the results assuming a 15 km locking depth in Figure 14. The deeper locking depth in this case reduces the elastic thickness and increases the estimate of recurrence time on the northern Bay San Andreas fault. Although not shown here, the 15 km locking depth model fits the data as well as the 10 km locking depth model.

3.2. The 1906 Postseismic and San Francisco Bay Interseismic Data

[40] In section 3.1 our estimates of the Bay Area San Andreas fault slip rate and recurrence time were based entirely on the post-1906 strain rate data. We did not use the GPS data across the northern Bay which provides spatial coverage of the contemporary velocity field and includes the effects of the Hayward-Rodgers Creek and

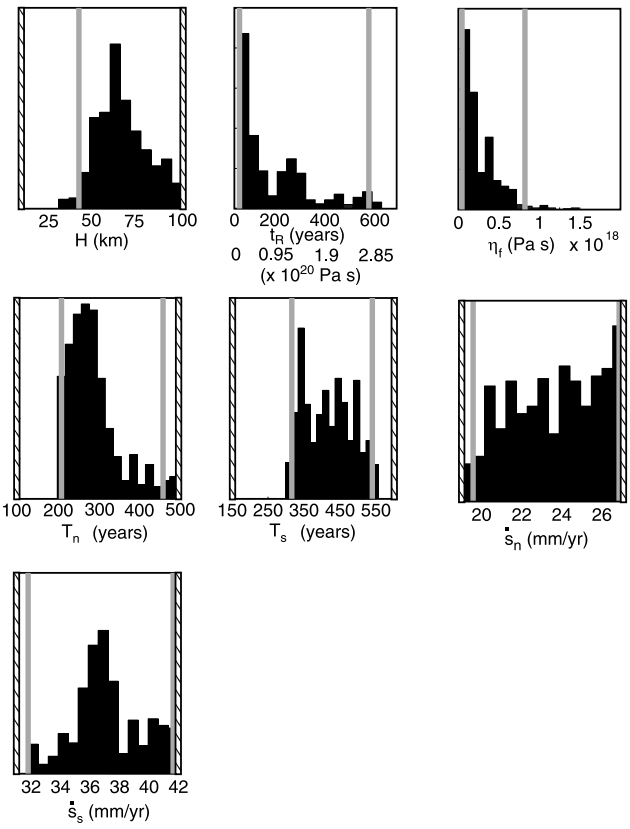

Figure 12. Probability distribution of parameters for Carrizo Plain/1906 inversion. Locking depth is 10 km. H is elastic thickness, t_R is relaxation time of asthenosphere, η_f is fault zone viscosity, T_n is northern Bay San Andreas fault recurrence time, $\dot{s}_n$ is northern Bay San Andreas fault slip rate, T_s is southern San Andreas fault (Carrizo) recurrence time, and $\dot{s}_n$ is southern San Andreas fault slip rate. Solid lines show 95% confidence intervals. Hatched lines show a priori bounds.

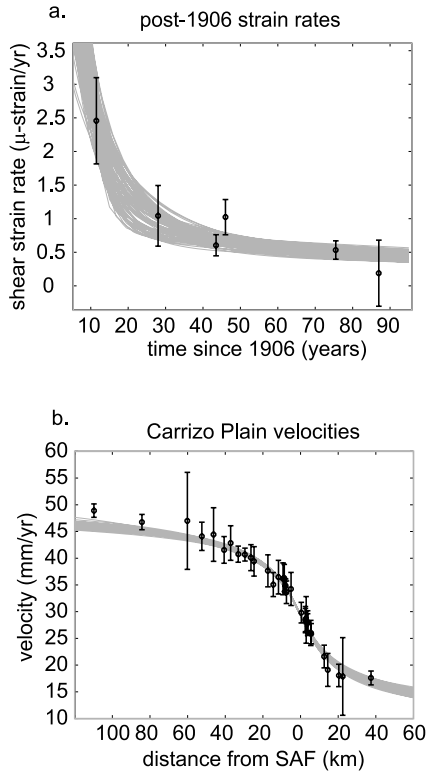

Figure 13. (a) Fit to post 1906 strain rate data using viscous-creep model. All models generated in Monte Carlo sampling are plotted. Error bars are 2σ. (b) Fit to Carrizo Plain data using viscous-creep model. All models generated in Monte Carlo sampling are plotted. Error bars are 2σ.

Concord-Green Valley faults. Now we perform a joint analysis of the post-1906 strain rate data and the San Francisco Bay GPS data. The San Andreas fault and Hayward fault are again approximated as infinitely long vertical strike-slip faults in an elastic layer over viscoelastic half-space. The San Andreas fault and Hayward fault are assumed to be locked interseismically down to 10 km depth and creep below 10 km in a viscous shear zone. We assume the same fault zone viscosity for the Hayward and San Andreas faults. To reduce the number of unknown fault parameters, we choose not to model viscous creep or viscoelastic coupling of the Concord-Green Valley fault. As by *Segall* [2002], we model the Concord-Green Valley fault kinematically as a dislocation buried at 10 km depth (Savage-Burford model, Figure 3a).

[41] We further assume that we can ignore mechanical interaction between the three faults. That is, we assume the stress perturbations generated by a fault do not greatly influence creep below the seismogenic zone on the neighboring faults. Interaction would effect the timing of earthquakes; however, this is fixed in the cycle models under consideration. While we could include stress interactions among neighboring faults using the boundary element method, it would require much more computation time since we would have to compute the time over which the pattern of cyclic motion on all the faults repeats and integrate the stresses over this group recurrence time. The group recurrence time could be much longer than the recurrence times on individual faults. To test the assumption that we can ignore stress interaction between faults, we calculated the shear stress at depth as a function of distance from the fault. Figure 15 shows stresses at 20 km depth due to slip on the San Andreas fault using the constant-creep model with D = 10 and H = 40. The stresses on the Hayward fault and Concord-Green Valley fault are more than one order of magnitude smaller than the stresses immediately next to the San Andreas fault. Thus the creep on each fault will be dictated primarily by the local perturbed stresses generated by the fault itself. This process of stress interaction following large earthquakes was investigated in detail by *Kenner and Segall* [1999], among others.

[42] As in the previous analysis, we invert this data with a priori bounds on parameters as listed in Table 3 using the Bayesian formulation of the inverse problem (equation (24)). The lower bounds on elastic thickness and locking depth are the same as in the previous inversion. Lower bounds on T_{SAF}, t_H, and T_H come from the historical record. The upper bounds on T_{SAF} and T_H are set such that coseismic slip is not excessively large. The bounds on slip rates are based loosely on the *WGCEP* [1999] study. The inversion results are summarized in Table 4, the posterior distributions are summarized in Figures 16 and 17, and the fit to the data is shown in Figure 18.

[43] Comparing the result of this inversion (Table 4) with the results from the previous inversion (Table 2), we see that the estimates of H, t_R, η_f, and T_{SAF} are similar, though the

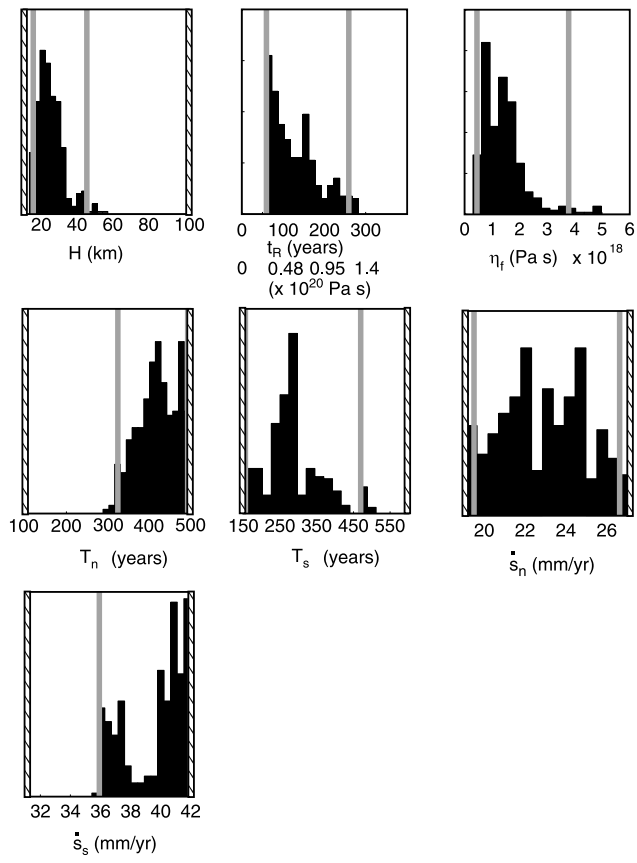

Figure 14. Same as Figure 12 with 15 km locking depth.

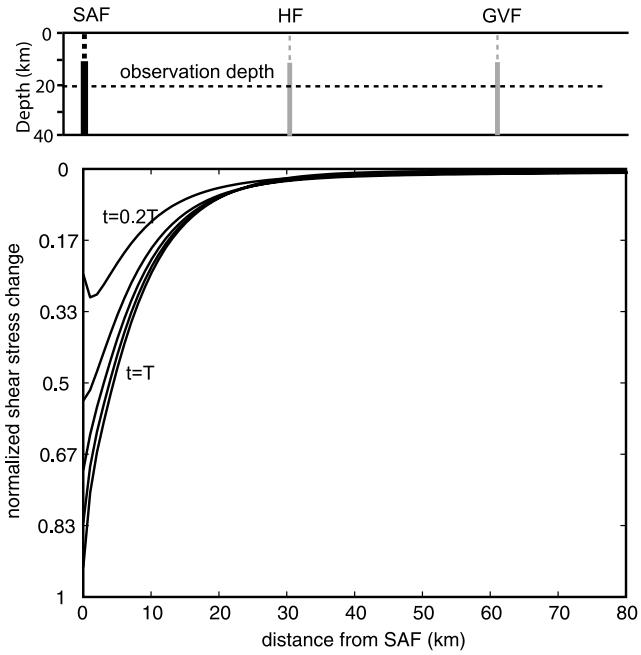

Figure 15. San Andreas induced cumulative shear stress change as a function of position at 20 km depth at 5 regularly spaced time intervals. $H = 40$,$D = 10$, $T = 2t_R$. Except immediately after the earthquake, the shear stress on the Hayward and Concord-Green Valley faults is more than an order of magnitude smaller than the stresses near the San Andreas fault. This result is the basis for ignoring the interaction of stresses on the three faults. SAF, San Andreas fault; HF, Hayward fault; GVF, Concord-Green Valley fault.

distribution on elastic thickness is shifted lower in this inversion. The 95% confidence interval on the San Andreas fault slip rate is again quite broad, but the distribution is skewed toward the upper end with a most probable slip rate of about 24 mm/yr. The Hayward slip rate of 10–13 mm/yr is well resolved within the a priori bounds. The recurrence times are also well resolved within the a priori bounds. The San Andreas recurrence time is in the range 188–315 years, and the Hayward recurrence time is in the range 469–700 years.

[44] For comparison, we show the results assuming a 15 km locking depth in Figure 17. The deeper locking depth in this case mainly influences the estimate of recurrence time on the San Andreas fault, pushing the recurrence time higher by about 100 years. Although not shown here, the 15 km locking depth model fits the data as well as the 10 km locking depth model (Figure 18).

Table 3. A Priori Bounds for Northern Bay

Parameter	Symbol	Minimum	Maximum
Elastic thickness	H	10	100
Locking depth, km	D	10	100
Half-space relaxation time, years	t_R	none	500
Fault zone viscosity per unit width	η_f	none	none
SAF recurrence interval, years	T_{SAF}	100	500
Hayward recurrence interval, years	T_H	225	700
Time since last Hayward earthquake, years	t_H	225	690
SAF slip rate, mm/yr	$\dot{s}_{\mathrm{SAF}}$	19	27
Hayward slip rate, mm/yr	$\dot{s}_H$	7	13
Green Valley slip rate, mm/yr	$\dot{s}_{GV}$	2	8

Table 4. Inversion Results - Northern Bay

Parameter	A Priori	95% Confidence	Most Probable
H, km	10–100	23–65	45
t_R, years	none	45–630	180 (9.0×10^{19})
η_f, Pa s/m	none	$(0.8–6.2) \times 10^{18}$	1.5×10^{18}
T_{SAF}, years	100–500	188–315	250
T_H, years	225–700	469–700	700
t_H, years	225–690	229–422	229
$\dot{s}_{\mathrm{SAF}}$, mm/yr	19–27	20.6–26.7	24.0
$\dot{s}_H$, mm/yr	7–13	9.9–13.0	12.8
$\dot{s}_{GV}$, mm/yr	2–8	8.0–8.0	8.0

4. Discussion

[45] Table 5 summarizes the results from this and other studies. The values for H, t_R, and η_f come from the Carrizo Plain/post-1906 inversion and the values for T_{SAF} and $\dot{s}_{\mathrm{SAF}}$ are taken from the second inversion which included the northern Bay area GPS data. The ranges of estimates of

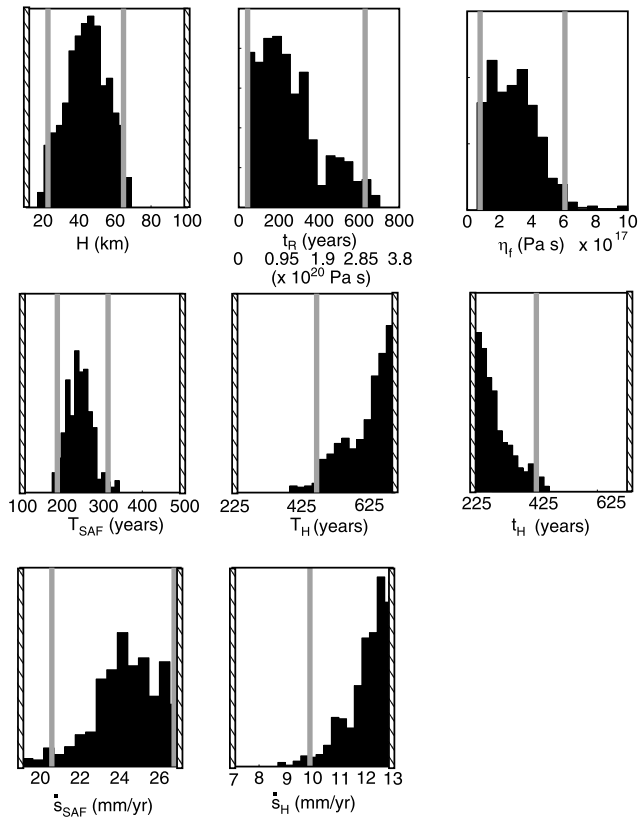

Figure 16. Probability distribution of parameters for northern San Francisco Bay data. Locking depth is 10 km. H is elastic thickness, t_R is relaxation time of asthenosphere, η_f is fault zone viscosity, T_{SAF} is northern Bay San Andreas fault recurrence time, T_H is Hayward fault recurrence time, t_H is time since last Hayward fault earthquake, $\dot{s}_{\mathrm{SAF}}$ is northern Bay San Andreas fault slip rate, $\dot{s}_H$ is Hayward fault slip rate, and $\dot{s}_{GV}$ is Concord-Green Valley fault slip rate. Solid lines show 95% confidence intervals. Hatched lines show a priori bounds.

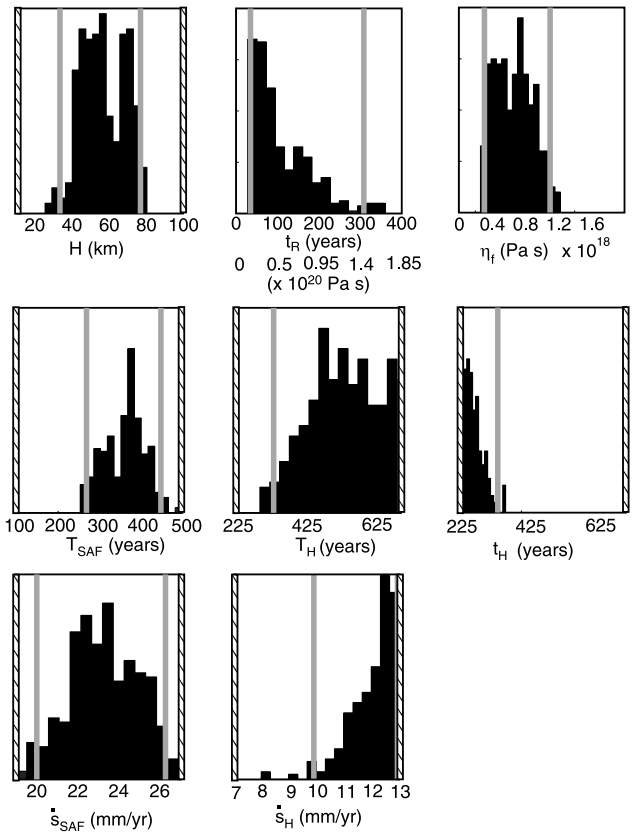

Figure 17. Same as Figure 16 with 15 km locking depth.

elastic thickness and relaxation time are notably larger in this study than in the *Segall* [2002] study using the no-creep model. This difference can be accounted for by the relatively low viscosity of the shear zone in the viscous-creep model. With creep in the viscous shear zone, the data are fit with a thicker elastic plate and longer half-space relaxation time than without the shear zone. There are no independent estimates of fault zone viscosity, but the estimate in this study is in good agreement with the estimate of *Kenner and Segall* [2003]. While this is expected given that the same data were used in both studies, it is encouraging that our viscous-creep cycle model, which incorporates postseismic and interseismic strain accumulation, predicts similar fault zone viscosity as the purely postseismic model of *Kenner and Segall* [2003]. The slip rate estimates from this study are in reasonable agreement with *Prescott et al.* [2001] estimates using the simpler Savage-Burford buried dislocation model but were fairly tightly constrained by a priori information.

[46] We can compare coseismic slip estimates from our model with field measurements of coseismic slip from recent large earthquakes. Figure 19 shows the probability distribution of coseismic slip for Carrizo Plain and San Francisco Bay San Andreas fault as well as the Hayward fault. The range of slip, 4.75–7.25 m, for the northern Bay San Andreas fault is larger than surface measurements typically in the range 2.5–4.5 m following the 1906 earthquake [*Lawson*, 1908] and is in better agreement with the *Thatcher et al.* [1997] estimate of coseismic slip from geodetic data ranging from 2.7 to 8.6 m. The Carrizo Plain coseismic slip estimate of 10.5–17.5 m is in good agreement with 11.0 ± 2.5 m of displacement that occurred across that fault in the 1857 earthquake in the Carrizo Plain according to *Grant and Sieh* [1994]. The coseismic slip on the Hayward fault is substantially greater than 2 m inferred for the 1868 earthquake by *Yu and Segall* [1996] which ruptured south of the geodetic profile used in this study. This discrepancy almost certainly arises because the rupture length is on the order of 60 km, which is far too short to be described by our two-dimensional model.

[47] If we assume a rupture length for our modeled earthquake events, we can calculate earthquake magnitudes and compare with empirical scaling relationships between magnitude and surface rupture length. *Wells and Coppersmith* [1994] suggest magnitude, M_w, and rupture length, L, are related as

$$M_w = (1.16 \pm 0.07)\log(L) + (5.08 \pm 0.10). \quad (27)$$

Using this relationship, earthquakes on the northern or southern section of the San Andreas fault with a rupture length in the range 300–450 km would have a magnitude in the range M_w = 7.7–8.4. Assuming these rupture lengths, rupture depth of 10 km, and our estimates of coseismic slip (Figure 19), we get a range of M_w = 7.7–8.0 for the northern section of the San Andreas and M_w = 8.0–8.2 for the southern section, in good agreement with the empirical values. For the Hayward fault, with a rupture length in the range 40–60 km, the scaling relationship

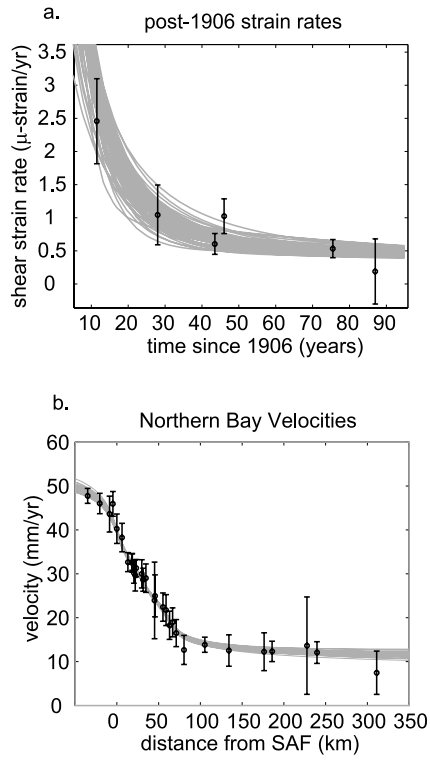

Figure 18. (a) Fit to post-1906 strain rate data using viscous-creep model. All models generated in Monte Carlo sampling are plotted. (b) Fit to northern Bay GPS data using viscous-creep model. All models generated in Monte Carlo sampling are plotted. Error bars are 2σ.

Table 5. Summary of Results From Various Studies

Parameter	This Paper (95% Interval)	*Segall* [2002] (90% Interval)	*Kenner and Segall* [2003]	*Prescott et al.* [2001] (95% Interval)
H, km	44–100	10–21	not resolved	
t_R, years	24–622	25–47	200 (assumed)	
η_f, Pa s/m	$(0.5–8.2) \times 10^{17}$		$(3.15–6.3) \times 10^{17}$	
T_{SAF} (northern Bay), years	188–315	130–368		
T_H, years	469–700	231–429		
t_H, years	229–422	225–348		
$\dot{s}_{SAF}$ (northern Bay), mm/yr	20.6–26.7	19–27		17–24.6
$\dot{s}_H$, mm/yr	9.9–13	7–13		5.1–15.5
$\dot{s}_{GK}$, mm/yr	8.0	5.4–8.0		4–12.4

gives magnitudes in the range M_w = 6.7–7.4. Again, using these same rupture lengths, rupture depth of 10 km, and our estimates of coseismic slip, our model magnitude for the Hayward fault is in the range M_w = 7.2–7.4. Thus, while the modeled Hayward slip events are larger than the observed 1868 event, the predicted magnitudes lie within the range of expected magnitude based on the empirical scaling relationship.

[48] *Knudsen et al.* [2002] have summarized paleoseismic estimates of timing of past earthquakes on the San Andreas fault north of San Francisco Bay. The penultimate event may have occurred 266–366 years before 1906, and an event prior to the penultimate may have occurred about 600 years before the 1906 event, suggesting a characteristic repeat time of about 300 years. This is at the upper end of our estimate of repeat time on the San Andreas fault. *Grant and Sieh* [1994] dated the penultimate event on the Carrizo Plain segment at about 350–450 years before the 1857 earthquake. A recurrence time of 350–450 years is within the 95% confidence interval of our estimate.

[49] We note here that we have not used any prior information from geology on the recurrence times of earthquakes. However, studies are emerging which provide good paleoseismic constraints on recurrence times. These studies construct probability density functions for the timing of past earthquakes with chronological modeling that incorporates historical and stratigraphic information and various dating techniques. Paleoseismic probability density functions of the dates of past earthquakes are available for the southern Hayward fault [*Lienkaemper et al.*, 2002], Frazier Mountain, near the Garlock fault [*Lindvall et al.*, 2002], and Pallett Creek and Wrightwood sites at the southern end of the 1857 rupture [*Fumal et al.*, 2002; *Biasi et al.*, 2002]. Using these tighter constraints on recurrence times as prior information would likely improve our ability to resolve parameters. In future work we will use such geologic data as prior information.

5. Conclusions

[50] We have developed boundary element models of postseismic and interseismic creep on the downward extension of coseismic rupture on strike-slip faults. Unlike the kinematic constant-creep coupling model of *Savage and Prescott* [1978], creep in the boundary element models is driven by shear stresses acting on the fault. Creep is driven by coseismic stress changes on the fault, rapid postseismic relaxation of the viscous asthenosphere, and steady interseismic loading by far-field motion of the plates.

[51] We developed two stress-driven creep models. In the constant-stress model the fault creeps at a constant (or zero) resistive shear stress. In the viscous-creep model the fault creeps in a linear viscous shear zone. In both stress-driven models, uniform coseismic slip is imposed down to the locking depth, D at regular intervals. The models produce different patterns of coseismic and interseismic slip. In the constant-stress model the entire depth of the fault is ruptured coseismically. From depth D to the bottom of the elastic plate, the slip tapers from the maximum at the top to zero on the bottom. During the interseismic period the deep part of the fault creeps to catch up with the amount of coseismic slip on the seismogenic part of the fault. At the end of the cycle the slip is uniform along the entire depth of the fault. In the viscous-creep model the lower part of the fault does not rupture coseismically. Instead, there is rapid postseismic afterslip immediately below the coseismic rup-

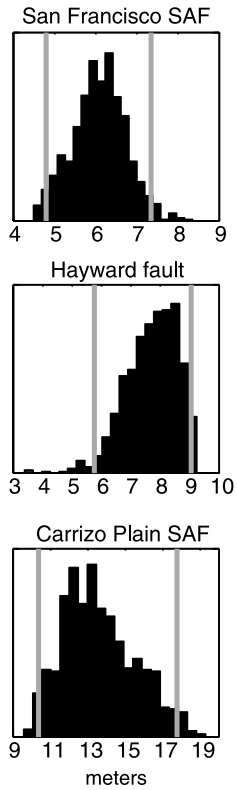

Figure 19. Posterior probability distributions of coseismic slip. Vertical lines are 95% confidence intervals.

ture as well as interseismic creep below depth D in response to relaxation of the viscous half-space and interseismic loading.

[52] We performed Bayesian inversions of triangulation and GPS data across the San Andreas fault using a priori information for slip rates and recurrence times. We demonstrated that it is not necessary to introduce different Earth rheology in northern and southern California in order to fit the northern Bay post-1906 strain rate data and the Carrizo Plain GPS data as suggested by *Segall* [2002] using the standard Savage-Prescott no-creep model. The high strain rates following the 1906 earthquake are reproduced in this model with creep in a viscous shear zone with viscosity per unit fault zone width that is at least an order of magnitude lower than the asthenosphere viscosity. If one takes the position that the crustal structure and rheology are likely to be similar in northern and southern California, our results imply that it is necessary to reject the simplest viscoelastic coupling model in favor of one that includes postseismic creep. Furthermore, we estimated slip rates and recurrence intervals on the Bay area faults that are consistent with estimates by *Segall* [2002] and *Prescott et al.* [2001] using simpler dislocation and no-creep coupling models.

[53] It is quite encouraging that despite the relative complexity of this model, the data are able to resolve many of the parameter values. This is particularly true for the rheological parameters. A lower bound of about 40 km is placed on the elastic thickness of the lithosphere and the asthenosphere and fault zone viscosities are both resolved to within an order of magnitude. The asthenosphere viscosity is on the order of 10^{19} Pa s (relaxation time of 30 years) and the fault zone viscosity per unit width is on the order of 10^{17} Pa s/m. The 95% confidence bounds on fault slip rates on the Carrizo Plain and northern San Francisco Bay sections of the San Andreas fault are not significantly smaller than the a priori bounds assumed from geological studies. However, the recurrence times on the Carrizo Plain and northern Bay San Andreas and Hayward faults are resolved to within about 100, 200, and 300 years, respectively.

Appendix A: Approximation for Infinite Sum

[54] *Savage* [1990] demonstrated that the velocity field produced at the ground surface in the viscoelastic coupling model can be duplicated with prescribed slip on vertical dislocations in an elastic half-space. This result is by virtue of the method of images used to derive the viscoelastic coupling solution. The solution for the surface displacements due to a dislocation in an elastic half-space extending from depth D_1 to D_2 is

$$v_H(x) = \frac{1}{\pi}\left[\tan^{-1}\left(\frac{x}{D1}\right) - \tan^{-1}\left(\frac{x}{D2}\right)\right]. \qquad \text{(A1)}$$

When comparing the form of equation (A1) with equation (3), it becomes clear that equations (1)–(4) represent a sum of dislocations extending from depth $D - 2nH$ to $D + 2nH$ with slip rate on each dislocation that is a function of time. Furthermore, *Savage* [1990] showed that the slip is approximately steady and equal to the plate rate for dislocations below about $7H$. Therefore equation (4) can be truncated after only a few terms with higher order terms approximated with steady slip on a buried dislocation in an elastic half-space.

[55] In the boundary element solution, the patches do not extend through the entire lithosphere, so we have to modify the Savage approximation. The solution for a fault with cyclic motion extending from depth D_1 to D_2 in an elastic layer over viscoelastic half-space is given by equations (4) and (5) with F_n replaced with

$$\begin{aligned} F_n(x, D2, H) - F_n(x, D1, H) = {} & \tan^{-1}\left(\frac{x}{2nH - D2}\right) \\ & - \tan^{-1}\left(\frac{x}{2nH + D2}\right) \\ & - \tan^{-1}\left(\frac{x}{2nH - D1}\right) \\ & + \tan^{-1}\left(\frac{x}{2nH + D1}\right). \end{aligned} \qquad \text{(A2)}$$

It follows that the equivalent half-space solution is the sum of dislocations extending from depths $2nH - D_2$ to $2nH - D_1$ and from $2nH + D_1$ to $2nH + D_2$. As before, equation (4) can be truncated after a few terms with higher order terms approximated by steady slip on a sum of dislocations sliding at the plate rate in an elastic half-space. Note that it is more efficient to calculate this sum than the double sum given in equations (4) and (5).

[56] **Acknowledgments.** We would like to thank Jim Savage, Arvid Johnson, Tom Parsons, and Elizabeth Hearn for reviews. This research was supported by the Southern California Earthquake Center. SCEC is funded by NSF Cooperative Agreement EAR-0106924 and USGS Cooperative Agreement 02HQAG0008. SCEC contribution 775.

References

Abromowitz, M., and I. A. Stegun (1970), *Handbook of Mathematical Functions*, Dover, Mineola, N.Y.

Biasi, G. P., R. J. Weldon, T. E. Fumal, and G. G. Seitz (2002), Paleoseismic event dating and the conditional probability of large earthquakes on the southern San Andreas fault, California, *Bull. Seismol. Soc. Am.*, *92*(7), 2761–2781.

Burgmann, R., S. Ergintav, P. Segall, E. Hearn, S. McClusky, R. Reilinger, H. Woith, and J. Zschau (2002), Time-dependent distributed afterslip on and deep below the Izmit earthquake rupture, *Bull. Seismol. Soc. Am.*, *92*(1), 126–137.

Fumal, T. E., I. R. J. Weldon, G. P. Biasi, T. E. Dawson, G. G. Seitz, W. T. Frost, and D. P. Schwartz (2002), Evidence for large earthquakes on the San Andreas fault at the Wrightwood, California, paleoseismic site: A.D. 500 to present., *Bull. Seismol. Soc. Am.*, *92*(7), 2726–2760.

Grant, L., and K. Sieh (1994), Paleoseismic evidence of clustered earthquakes on the San Andreas fault in the Carrizo Plain, California, *J. Geophys. Res.*, *99*, 6819–6841.

Hearn, E., R. Burgmann, and R. Reilinger (2002), Dynamics of Izmit earthquake postseismic deformation and loading of the Duzce earthquake hypocenter, *Bull. Seismol. Soc. Am.*, *92*(1), 172–193.

Henstock, T., A. Levander, and J. Hole (1997), Deformation in the lower crust of the San Andreas fault system in northern California, *Science*, *278*, 650–653.

Hsu, Y.-J., N. Bechor, P. Segall, S.-B. Yu, L.-C. Kuo, and K.-F. Ma (2002), Rapid afterslip following the 1999 Chi-Chi, Taiwan earthquake, *Geophys. Res. Lett.*, *29*(16), 1754, doi:10.1029/2002GL014967.

Jonsson, S., H. Zebker, P. Segall, and F. Amelung (2002), Fault slip distribution of the M_w 7.1 Hector Mine, California, earthquake, estimated from satellite radar and GPS measurements, *Bull. Seismol. Soc. Am.*, *92*, 1377–1389.

Karato, S.-I., and P. Wu (1993), Rheology of the upper mantle: A synthesis, *Science*, *260*, 771–778.

Kenner, S., and P. Segall (1999), Time-dependence of the stress shadowing effect and its relation to the structure of the lower crust, *Geology*, *27*(2), 119–122.

Kenner, S. J., and P. Segall (2003), Lower crustal structure in northern California: Implications from strain rate variations following the 1906

San Francisco earthquake, *J. Geophys. Res.*, *108*(B1), 2011, doi:10.1029/2001JB000189.

Knudsen, K. L., R. C. Witter, C. E. Garrison-Laney, J. N. Baldwin, and G. A. Carver (2002), Past earthquake-induced rapid subsidence along the northern San Andreas fault: A paleoseismological method for investigating strike-slip faults, *Bull. Seismol. Soc. Am.*, *92*(7), 2612–2636.

Lapusta, N., J. R. Rice, Y. Ben-Zion, and G. T. Zheng (2000), Elastodynamic analysis for slow tectonic loading with spontaneous rupture episodes on faults with rate- and state-dependent friction, *J. Geophys. Res.*, *105*(B10), 23,765–23,789.

Lawson, A. (1908), The California earthquake of April 18, 1906: Report of the State Earthquake Investigation Commission, technical report, Carnegie Inst. of Washington, Washington, D. C.

Li, V., and J. Rice (1987), Crustal deformation in great California earthquake cycles, *J. Geophys. Res.*, *92*(B11), 11,533–11,551.

Lienkaemper, J. J., T. E. Dawson, S. F. Personius, G. G. Seitz, L. M. Reidy, and D. P. Schwartz (2002), A record of large earthquakes on the southern Hayward fault for the past 500 years, *Bull. Seismol. Soc. Am.*, *92*(7), 2637–2658.

Lindvall, S. C., T. K. Rockwell, T. E. Dawson, J. G. Helms, and K. W. Bowman (2002), Evidence for two surface ruptures in the past 500 years on the San Andreas fault at Frazier Mountain, California, *Bull. Seismol. Soc. Am.*, *92*(7), 2689–2703.

Linker, M., and J. Rice (1997), Models of postseismic deformation and stress transfer associated with the Loma Prieta earthquake, in *The Loma Prieta, California Earthquake of October 17, 1989: Aftershocks and Postseismic Effects*, *U.S. Geol. Surv. Prof. Pap.*, *1550-D*, D253–D275.

Mathews, M., and P. Segall (1993), Estimation of depth-dependent fault slip from measured surface deformation with application to the 1906 San Francisco earthquake, *J. Geophys. Res.*, *98*, 12,153–12,163.

Mosegaard, K., and A. Tarantola (2002), Probabilistic approach to inverse problems, in *International Handbook of Earthquake and Engineering Seismology*, Part A, edited by W. H. K. Lee et al., pp. 237–265, Academic, San Diego, Calif.

Murray, M., J. Savage, M. Lisowski, and W. Gross (1993), Coseismic displacements: 1992 Landers, California, earthquake, *Geophys. Res. Lett.*, *20*, 623–626.

Nur, A., and G. Mavko (1974), Postseismic viscoelastic rebound, *Science*, *183*, 204–206.

Parsons, T. (1998), Seismic reflection evidence that the Hayward fault extends into the lower crust of the San Francisco Bay area, California, *Bull. Seismol. Soc. Am.*, *88*, 1212–1223.

Parsons, T. (2002), Post-1906 stress recovery of the San Andreas fault system calculated from three-dimensional finite element analysis, *J. Geophys. Res.*, *107*(B8), 2162, doi:10.1029/2001JB001051.

Parsons, T., and P. Hart (1992), Dipping San Andreas and Hayward fault revealed beneath San Francisco Bay, California, *Bull. Seismol. Soc. Am.*, *82*, 454–480.

Pollitz, F., C. Wicks, and W. Thatcher (2001), Mantle flow beneath a continental strike-slip fault: Postseismic deformation after the 1999 Hector Mine earthquake, *Science*, *293*, 1814–1818.

Prescott, W., J. Savage, J. Svarc, and D. Manaker (2001), Deformation across the Pacific-North America plate boundary near San Francisco, California, *J. Geophys. Res.*, *106*, 6673–6682.

Reches, Z., G. Schubert, and C. Anderson (1994), Modeling of periodic great earthquakes on the San Andreas fault: Effects of nonlinear crustal rheology, *J. Geophys. Res.*, *99*, 21,983–22,000.

Savage, J. (1990), Equivalent strike-slip earthquake cycles in half-space and lithosphere-asthenosphere earth models, *J. Geophys. Res.*, *95*, 4873–4879.

Savage, J., and R. Burford (1973), Geodetic determination of relative plate motion in central California, *J. Geophys. Res.*, *78*, 832–845.

Savage, J., and W. Prescott (1978), Asthenosphere readjustment and the earthquake cycle, *J. Geophys. Res.*, *83*, 3369–3376.

Segall, P. (2002), Integrating geologic and geodetic estimates of slip rate on the San Andreas fault system, *Int. Geol. Rev.*, *44*, 62–82.

Sieh, K., and R. Jahns (1984), Holocene activity of the San Andreas fault at Wallace Creek, California, *Geol. Soc. Am. Bull.*, *95*, 883–896.

Thatcher, W., G. Marshall, and M. Lisowski (1997), Resolution of fault slip along the 470-km-long rupture of the great 1906 San Francisco earthquake and its implications, *J. Geophys. Res.*, *102*, 5353–5367.

Turcotte, D., and D. Spence (1974), An analysis of strain accumulation on a strike-slip fault, *J. Geophys. Res.*, *79*, 4407–4412.

Wells, D. L., and K. J. Coppersmith (1994), New empirical relationships among magnitude, rupture length, rupture width, rupture area, and surface displacement, *Bull. Seismol. Soc. Am.*, *84*(4), 974–1002.

Working Group on California Earthquake Probabilities (WGCEP) (1999), Earthquake probabilities in the San Francisco Bay region: 2000 to 2030-a summary of findings, *U.S. Geol. Surv. Open File Rep.*, *99-517*, 60 pp.

Yu, E., and P. Segall (1996), Slip in the 1868 Hayward earthquake from the analysis of historical triangulation data, *J. Geophys. Res.*, *101*(B7), 16,101–16,118.

Zhu, L. (2000), Crustal structure across the San Andreas fault, southern California from teleseismic converted waves, *Earth Planet. Sci. Lett.*, *179*, 183–190.

K. M. Johnson and P. Segall, Geophysics Department, Stanford University, Mitchell Building 360, Stanford, CA 94305, USA. (kaj@pangea.stanford.edu; segall@stanford.edu)